Article

Cell Reports

Cellular Barcoding Identifies Clonal Substitution as a Hallmark of Local Recurrence in a Surgical Model of Head and Neck Squamous Cell Carcinoma

Graphical Abstract

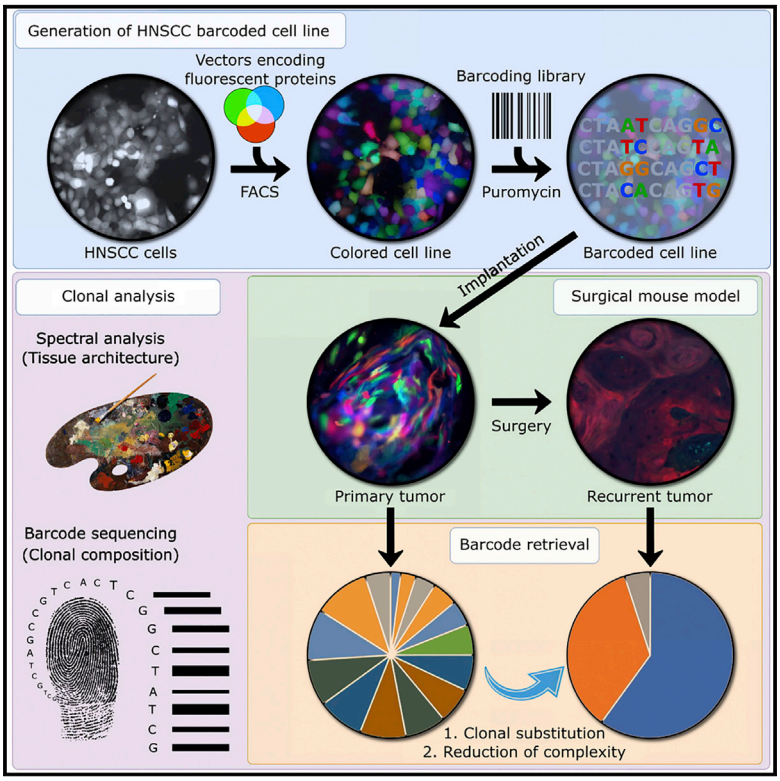

Highlights

- Xenografted HNSCC comprises multiple unevenly propagating clones
- Postsurgical recurrences reproducibly show a substitution of dominating clones
- Clones enriched in recurrences are initially sparse in primary tumors
- Clones enriched in recurrences feature distinct phenotypic and genetic traits

Authors

Vincent Roh, Pierre Abramowski, Agnès Hiou-Feige, ..., Boris Fehse, Christian Simon, Genrich V. Tolstonog

Correspondence

fehse@uke.de (B.F.), christian.simon@chuv.ch (C.S.), genrich.tolstonog@chuv.ch (G.V.T.)

In Brief

Roh et al. combine fluorescent protein marking and cellular barcoding to investigate the clonal composition of matched primary and recurrent tumors in a surgical model of HNSCC. They demonstrate that clones present in primary tumors are substituted by other initially rare clones expanding after resection.

Roh et al., 2018, Cell Reports *25*, 2208–2222
November 20, 2018
https://doi.org/10.1016/j.celrep.2018.10.090

CellPress

OPEN ACCESS
CellPress

Cell Reports
Article

Cellular Barcoding Identifies Clonal Substitution as a Hallmark of Local Recurrence in a Surgical Model of Head and Neck Squamous Cell Carcinoma

Vincent Roh,[1] Pierre Abramowski,[2,8,10] Agnès Hiou-Feige,[1,8] Kerstin Cornils,[2,8] Jean-Paul Rivals,[1,9] Alexandre Zougman,[3] Tim Aranyossy,[2] Lars Thielecke,[4] Zinnia Truan,[1] Maxime Mermod,[1] Yan Monnier,[1] Vladimir Prassolov,[5] Ingmar Glauche,[4] Ali Nowrouzi,[6,7] Amir Abdollahi,[6,7] Boris Fehse,[2,*] Christian Simon,[1,*] and Genrich V. Tolstonog[1,11,*]

[1]Department of Otolaryngology – Head and Neck Surgery, University Hospital of Lausanne, Lausanne, Switzerland
[2]Research Department Cell and Gene Therapy, Department of Stem Cell Transplantation, University Medical Center Hamburg-Eppendorf (UKE), Hamburg, Germany
[3]Clinical and Biomedical Proteomics Group, Cancer Research UK Centre, Leeds Institute of Cancer and Pathology, St. James's University Hospital, Leeds, UK
[4]Institute for Medical Informatics and Biometry, Faculty of Medicine Carl Gustave Carus, Technische Universität Dresden, Dresden, Germany
[5]Engelhardt Institute of Molecular Biology, Russian Academy of Sciences, Moscow 119991, Russia
[6]German Cancer Consortium (DKTK), Translational Radiation Oncology, German Cancer Research Center (DKFZ), Core Center Heidelberg, Heidelberg, Germany
[7]Division of Molecular and Translational Radiation Oncology, Heidelberg University Hospital (UKHD) and DKFZ, Heidelberg Institute of Radiation Oncology (HIRO), National Center for Radiation Research in Oncology (NCRO), Heidelberg, Germany
[8]These authors contributed equally
[9]Present address: Department of Oncology, University Hospital of Lausanne, Lausanne, Switzerland
[10]Present address: Miltenyi Biotec, Bergisch Gladbach, Germany
[11]Lead Contact
*Correspondence: fehse@uke.de (B.F.), christian.simon@chuv.ch (C.S.), genrich.tolstonog@chuv.ch (G.V.T.)
https://doi.org/10.1016/j.celrep.2018.10.090

SUMMARY

Local recurrence after surgery for head and neck squamous cell carcinoma (HNSCC) remains a common event associated with a dismal prognosis. Improving this outcome requires a better understanding of cancer cell populations that expand from postsurgical minimal residual disease (MRD). Therefore, we assessed clonal dynamics in a surgical model of barcoded HNSCC growing in the submental region of immunodeficient mice. Clonal substitution and massive reduction of clonal heterogeneity emerged as hallmarks of local recurrence, as the clones dominating in less heterogeneous recurrences were scarce in their matched primary tumors. These lineages were selected by their ability to persist after surgery and competitively expand from MRD. Clones enriched in recurrences exhibited both private and shared genetic features and likely originated from ancestors shared with clones dominating in primary tumors. They demonstrated high invasiveness and epithelial-to-mesenchymal transition, eventually providing an attractive target for obtaining better local control for these tumors.

INTRODUCTION

Local recurrences after surgical removal of the primary tumor are generally, and in particular in head and neck squamous cell carcinoma (HNSCC) (Gath and Brakenhoff, 1999), suspected to originate from minimal residual disease (MRD) left behind during initial surgery. Cancer cells that have expanded beyond the margin of the tumor as a consequence of the acquisition of an invasive phenotype may potentially survive after therapy and resume growth, giving rise to local recurrence. Some similarities with cancer stem cells (CSCs) could be anticipated, because the latter also have the ability to undergo an invasion-associated epithelial-mesenchymal transition (EMT) and repopulate tumors (Ye and Weinberg, 2015). The CSC model would imply that recurrent tumors originate from a subset of CSCs likely exhibiting more invasive properties and thus causing a more aggressive disease than the primary tumor. In this respect, there is a striking parallel with metastatic progression, which also relies on the acquisition of an invasive phenotype (Liotta, 2016; Talmadge and Fidler, 2010). Metastases, as suggested by experimental work, appear to be driven by a stem-like cell subpopulation preferentially seeding and growing at metastatic niches (Liotta, 2016; Talmadge and Fidler, 2010). The concept of rare metastasis-forming (Talmadge and Fidler, 2010) or metastasis-initiating cells (Celià-Terrassa and Kang, 2016), which are related to CSCs, could be hypothetically applied to recurrences. If true, local recurrences could be initiated by rare CSC-like clones pre-existing within the heterogeneous cancer cell population, disseminating alone or as a collective (Cheung and Ewald, 2016) and undergoing an evolutionary diversification (Turajlic and Swanton, 2016). In this context, the rapidly developing concept of clonal heterogeneity (McGranahan and Swanton, 2017) would explain the phenotypic evolution from a primary to a recurrent tumor by surmising that a handful of clones within the primary cancer cell population will disseminate and outgrow after surgery.

Squamous cell carcinomas of the head and neck are aggressive and deadly cancers (Marur and Forastiere, 2016) annually affecting more than half a million people worldwide (Global Burden of Disease Cancer Collaboration et al., 2017). The treatment for these cancers typically consists of surgical removal, followed by various adjuvant treatments, such as radiation therapy alone or in combination with chemotherapy. This cancer is well known for its capacity to locally recur, and it is undisputed that these local recurrences are among the main reasons for patient mortality (Gleber-Netto et al., 2015). Thus, HNSCC serves as an excellent model to study the biology of local recurrences after surgery. If locally recurring HNSCC truly originates from few or single clones, adjuvant treatment of patients can be potentially improved by combining non-specific therapies with a targeted approach to specifically eliminate these cells.

To study local recurrence at a single-cell resolution, we developed a surgical model of HNSCC recurrence using red-green-blue (RGB)-marked, genetically barcoded human cancer cells (CAL27) able to grow invasively in the submental region of immunodeficient mice. CAL27 cells were lentivirally labeled with a combination of three fluorescent proteins (RGB panel) (Weber et al., 2011), followed by DNA barcoding using a highly complex lentiviral library (Thielecke et al., 2017). While fluorescent proteins helped with image-guided surgery and were used to approximate clonal composition by microscopy, genetic barcodes permitted a precise clonal deconvolution using next-generation sequencing (NGS). Using this technology, we exhaustively analyzed the cellular population contributing to local relapses in HNSCC.

RESULTS

RGB Marking and Genetic Barcoding to Study Tumor Clonality in a Mouse Model of Postsurgical HNSCC Recurrence

The RGB-marked, barcoded CAL27 cell line (RGB32) was generated in two steps: a first large-scale transduction of CAL27 cells with a mixture of mCherry, Venus, and Cerulean fluorescent vectors resulted in the CRGB cell line, which was then modified by a second large-scale transduction with the BC32 barcode library followed by puromycin selection. The small proportion of barcode overlap between barcode sequencing (Bar-Seq) replicates after retrieval from 200 ng of genomic DNA (corresponding to $\sim 3 \times 10^4$ cells) confirmed the high barcode diversity in the RGB32 population (Figures S1A and S1B). *In vitro* culture of RGB32 cells resulted in an enrichment of a subset of barcodes, as shown by the frequency of the most dominant barcode in each population increasing from 0.18% to 0.54% and 2.70% after 1, 10, or 20 passages, respectively (Figure S1C). To completely avoid any potential expansion bias *in vitro*, only early passage RGB32 cells (p.2) were implanted in mice either alone or together with HNSCC patient-derived cancer-associated fibroblasts (CAFs), known for their ability to promote tumor growth and metastasis (Wheeler et al., 2014).

Upon implantation in the submental region of NMRI/nude mice, RGB32 tumors showed HNSCC's typical squamous differentiation (Figure 1A) and a tendency toward increased growth rate in the group with CAF co-implantation (Figure 1B, top). Taking advantage of RGB colors, we performed image-guided microsurgeries (Figure 1C) to resect tumors as completely as possible, although potentially leaving behind MRD as presumed from the histological evaluation of sagittal sections from tumor-bearing floor-of-the-mouth (FOM) (Figure 1A). Palpable recurrences started to grow in the majority (9/12) of operated mice 3–6 weeks after surgery. In this cohort, no lymph node (LN) metastasis or pulmonary metastasis was observed in recurrent-tumor bearing mice. The growth kinetics of recurrent tumors developing in the group of mice without human CAF co-implantation was very consistent, in contrast to the group with co-implanted CAFs that showed more diverse patterns of recurrent tumor growth (Figure 1B, bottom).

Spectral Analysis Shows Reduced Heterogeneity in Recurrent Tumors and Suggests Clonal Substitution after Surgery

Live fluorescence imaging showed that primary tumors were fragmented into differently colored areas and more heterogeneous than recurrent tumors (Figure S2A), thus hinting at potential clonal reduction after surgery. Next, sections from a set of eight matching primary and recurrent tumor pairs were imaged by fluorescence microscopy, demonstrating patterns of diverse multicolored cellular areas in primary tumors, whereas recurrent tumors usually consisted of few dominant colors organized in larger patches (Figures 2A and S2B). Predictably, cell lines explanted from a set of recurrent tumors retained the colors of the dominant patches found in the tumor they originated from (Figure 2A). In addition, the diversity of colors was noticeably greater in differentiated areas (Figure 2B), indicating that a large fraction of color-coded cells underwent terminal squamous differentiation. Computer-assisted spectral deconvolution of the previous images (Figures 2C, 2D, and S2C) revealed a surprisingly high proportion of pixels colored with a hue specifically enriched in the recurrent tumors (up to 25.2%), suggesting that their cellular composition had profoundly changed after surgery (Figure 2D). At the tumor front and in the surrounding normal tissue, several instances of lymphovascular invasion (LVI) by apparently monoclonal groups of cancer cells were observed (Figures 2E and 2F). In addition, the peritumoral area of the tumor seemed more homogeneous than the intratumoral area, as reflected by the limited number of colors displayed by the clones located at the tumor border (Figures 2E and 2G). These clones found inside lymphatics and at the tumor border are likely candidates remaining after surgery and contributing to recurrences.

Bar-Seq Confirms Substitution of Dominating Clones after Postsurgical Tumor Regrowth

Quantification of barcodes by Bar-Seq revealed that the diversity of clones (defined as the progeny of a single *founder cell* which carries a unique barcode) found in primary tumors represented on average 9.0% of the diversity of barcodes in the RGB32 reference cell line (mean = 9.0%; SD = 6.6%). This number further decreased to about 0.2% of the reference in recurrent tumors (mean = 0.21%; SD = 0.07%), indicating a stepwise and drastic reduction of the clonal diversity from the original cell line to primary and recurrent tumors (Figure 3A). Notably, co-implantation of CAFs (1×10^6 cells) slightly increased clonal heterogeneity in

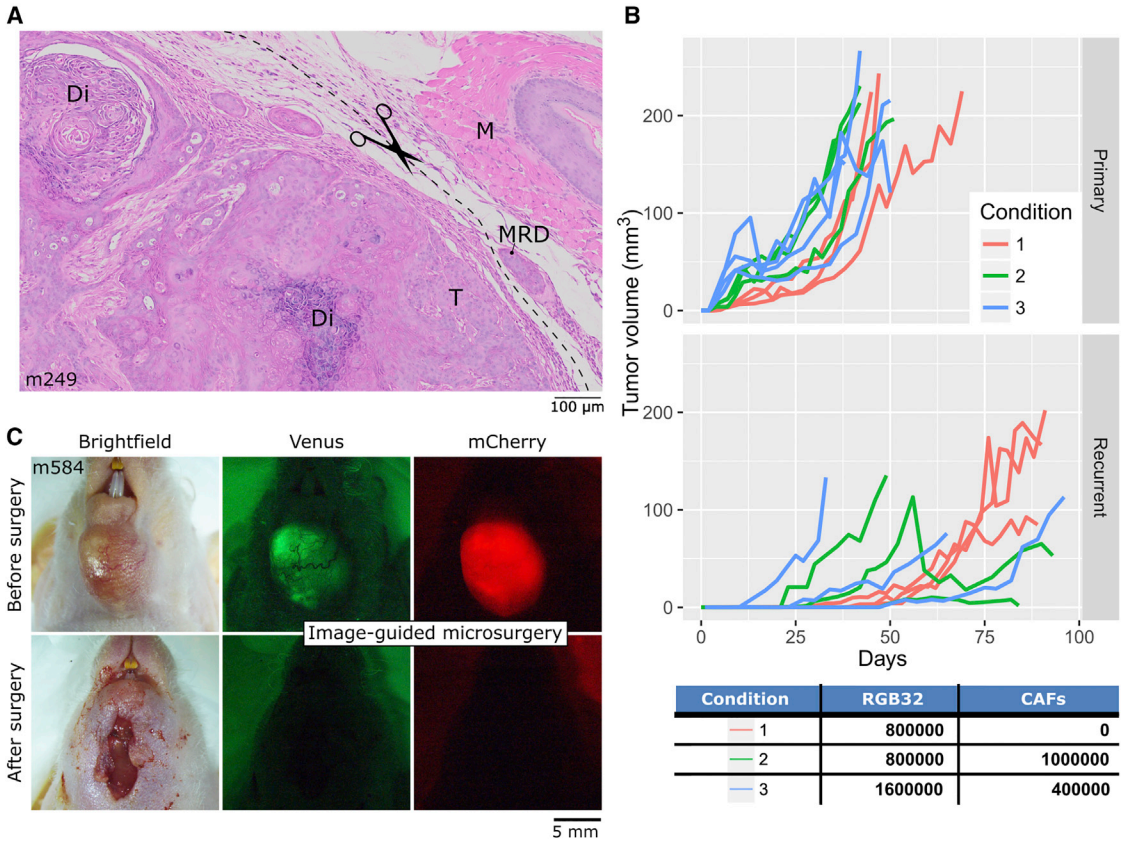

Condition	RGB32	CAFs
1	800000	0
2	800000	1000000
3	1600000	400000

Figure 1. Surgical Mouse Model for Recurrent HNSCC

(A) H&E staining of a floor-of-the-mouth (sagittal section) from a RGB32 tumor-bearing mouse. T, tumor; Di, areas of squamous differentiation; MRD, minimal residual disease, which stays with the adjacent muscular (M) tissue.

(B) Growth of primary (top panel) and recurrent tumors (bottom panel) following cell implantation and surgery. The number of implanted cells is indicated in the bottom table (by cohort).

(C) The expression of fluorescent proteins by cancer cells allows sensitive control of the residual cells during and after image-guided microsurgery. See also Figure S1 for details on the characterization of the RGB32 cell line.

the corresponding group, raising the mean complexity from 9.0% to 19.0% (mean = 19.0%; SD = 11.4%) (Figure 3A). Similar results were obtained when co-implanting CAFs (4×10^5) with a higher number of implanted RGB32 cells (1.6×10^6) (Figure 3A). Occurrence of the most abundant clone (first rank) in each primary tumor (n = 8) varied from 3.2% to 31.2%, whereas it represented between 32.9% up to 99.6% of the whole sample population in recurrent tumors (n = 8) (Figure 3B; left). Strikingly, the first-ranked clone in each recurrent tumor was always different from the first-ranked clone in the matched primary tumor (Figure 3B; right), demonstrating that clonal substitution invariably happened during the outgrowth of recurrent tumors. Bar graphs displaying the relative frequency (in percent of the whole population) of the top-five ranked barcodes found in each sample give a sense of the clonal type of each tumor (Figures S3A–S3H). In 4 of 8 recurrent tumors, we observed the extreme overrepresentation of a single, yet always different barcode (Figures S3A, S3B, S3E, and S3G). The barcode composition from three explant cell lines accurately reproduced the composition of their matching recurrent tumor (Figures S3F–S3H), even though we observed marginal expansion of some other clones (Table S1). This suggests that a number of "passenger" clones, including clones prevailing in primary tumors, were carried over into recurrent tumors and can be reactivated by *in vitro* culture of explant cell lines.

Next, we combined Bar-Seq data from eight primary and recurrent tumor pairs in a global analysis and included barcodes with total counts per million (CPMs) of at least 30,000 across samples (Figure 3C; Table S1). The presence of multicolored bars in this graph demonstrates that some clones (such as R10, R137, or R140; Figure 3C, top panel) proficiently grew in multiple primary tumors, which were all clonally more heterogeneous than recurrent tumors. Every largest clone in recurrences (Figure 3C, bottom panel) only dominated in a single sample and was clearly underrepresented in the respective primary tumors, with the exception of R12 and R3 that were ranked second (4.77%) and fifth (2.41%) in their primary tumor, though representing small fractions (Table S1). To functionally designate the founding cells of the dominating clones in primary and recurrent tumor samples, from here on we refer to them as tumor-initiating clones (TICs) or recurrent TICs (RTICs), respectively. Notably, several clones ranked first in recurrences were also detected, although in minor quantities, across multiple primary (e.g., R2

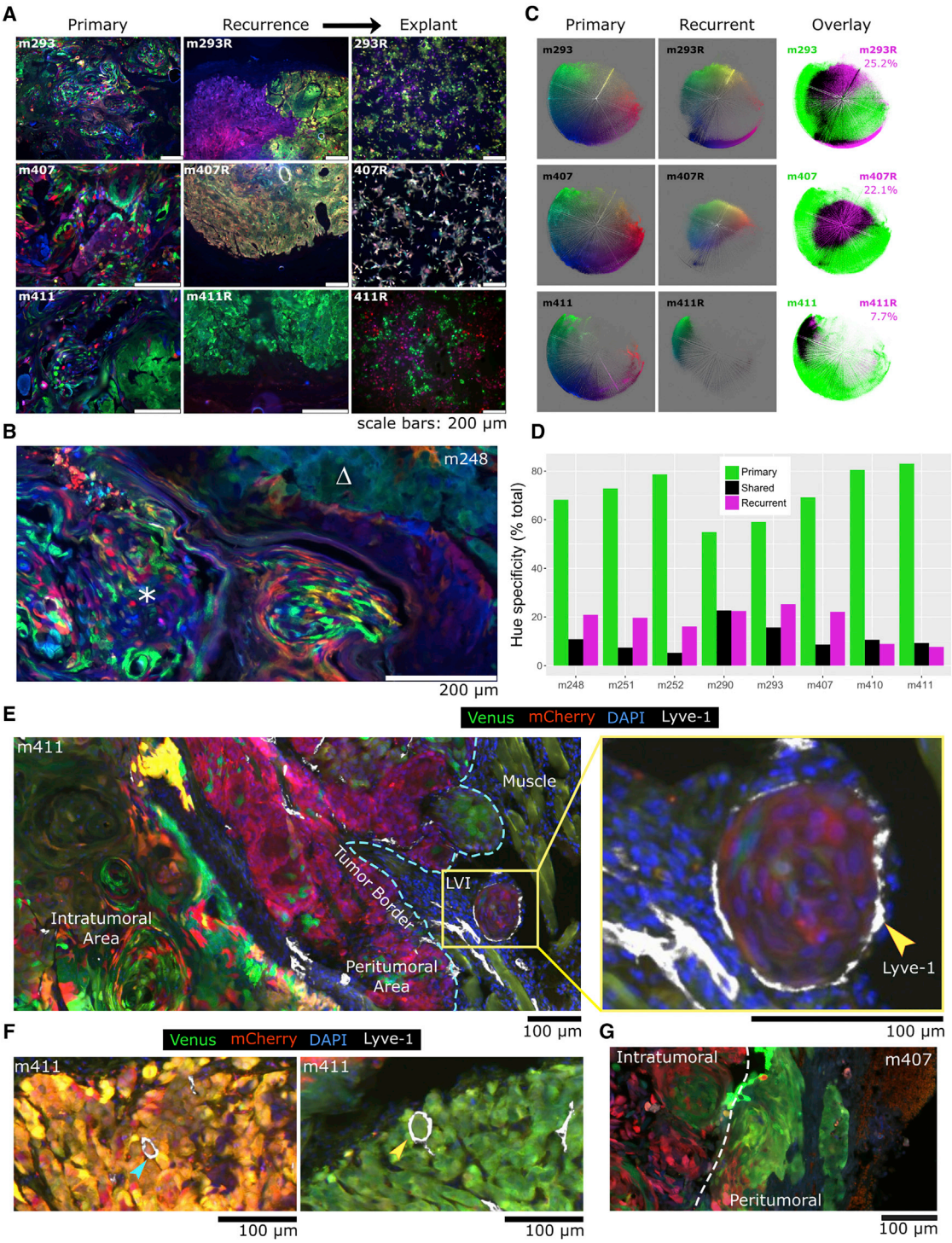

Figure 2. Spectral Analysis of Xenografted HNSCC Tumors

(A) Multicolor fluorescence microscopy of matched primary tumors (left), recurrent tumors (middle) and recurrence-derived explant cell lines (right).

(B) Higher magnification image of a representative primary tumor showing a highly diverse multicolor area of differentiation (asterisk) next to a more homogeneous non-differentiated area of the tumor (triangle).

(C) Spectral distribution of hues in microscopy images shown in (A). In these deconvolution plots, each pixel from the original picture is plotted according to its hue value (azimuthal coordinate) and its color saturation value (radial coordinate). Overlaying hues specific for primary or recurrent tumors after transformation in a green or a magenta mask respectively shows a high percentage of recurrence-specific hues.

(legend continued on next page)

in 5 and R12 in 8 tumors) or recurrent tumors (e.g., R3 in 6 and R12 in 8 tumors, but both were truly dominant in only one case) (Figure S3I). Thus, our data strongly suggest that certain competitive clones, which are usually underrepresented in primary tumor bulk, are equipotent to seed recurrent tumors.

Statistical Modeling of Tumor Resection

We raised the question whether and under which circumstances a subset of initially minor clones (RTICs) can ultimately dominate in the recurrent tumor. First, we statistically addressed this question by a quantitative estimation of the surgical process. Under the most naive assumption about the nature of the original tumor one could argue that all cells of all clones were equipotent and homogenously distributed. We approximated that only 1,000 cells remain from an initial tumor of 25×10^7 cells and further adhered to the conservative estimation that up to 25% of all cells represent potential RTICs (usually, we only observed a much smaller frequency), which are homogenously distributed in the initial tumor. Defining this setting as the null hypothesis (i.e., no spatial correlation of the clones), the extremely low probability $< 10^{-6}$ indicated that the enrichment of those RTICs to more than 80% in the recurrent tumor is virtually impossible only based on the sampling process (see details in the STAR Methods). Therefore, a homogenously mixed tumor could be excluded, while a spatial correlation of the seeding clones (including potential RTICs) appeared as a plausible alternative hypothesis. To further substantiate this notion in a second step, we contrasted the unlikely homogeneous scenario with an alternative setting in which clones are spatially confined but still, all cells are equipotent (Figure 3D). Using this schematic representation and sampling cells from the hypothetical MRD, the alternative scenario was much closer to the experimentally observed, reduced heterogeneity in recurrent tumors, while we found a distinctly higher clonal heterogeneity in the homogeneous scenario. This finding confirmed that random selection from a homogeneous mixture of equipotent clones is highly unlikely as a mechanism to promote the outgrowth of few RTICs, and that other mechanisms, like the spatial correlation of the seeding clones beyond the tumor periphery or a competitive growth advantage, need to be considered.

RTICs Are Enriched at the Primary Tumor Periphery and in the Tumor Beds

The observed distribution of color-coded cells in primary tumors suggests that some clones are more prominent at the tumor periphery (Figures 2E and 2G). These cells could include potential RTICs. To compare the clonal composition of peritumoral and intratumoral areas, we selected five primary tumors for which the composition of the recurrent tumor was already assessed by Bar-Seq and performed laser microdissection followed by Bar-Seq analysis. Next, we scored each retrieved barcode for being enriched in the peritumoral area and in recurrent tumor. Although tumor edges were found to be colonized by multiple clones, including those that prevailed in the tumor mass (e.g., R10), we observed a significant enrichment of R2, R3, and R12 RTICs at the edges of primary tumors (Figure 3E). However, being enriched does not mean that these clones were the most abundant at the tumor front. For example, R3 accounted for 0.44% of the peripheral clones in mouse m407, whereas the most abundant clone (R2594) was approximately a hundred times bigger (constituting 41% of all clones at the periphery) (Table S1). Yet after surgery, only R3 was found in m407R recurrent tumor, whereas none of the 11 more abundant clones at the periphery was detected. This proved that abundance at the edge was not sufficient to propagate into the recurrent tumor. It might be speculated that further dissemination is required to initiate recurrence, potentially through deeper invasion in surrounding tissue or LVI.

To find out which clones were seeding outside the tumors, we analyzed the clonal composition of seven primary tumors and matching underlying muscular layers of the FOM (i.e., surgical tumor beds) from RGB32-implanted mice. We expected to detect some clones previously identified as enriched in recurrent tumors. Barcodes that were detected in at least 2 of 7 tumor beds and had positive enrichment scores (log ratio between read counts in the tumor bed and the matched primary tumor) in at least one of them are presented in a heatmap (Figure 3F). As anticipated, R3 (RTIC previously identified in mouse m407) was enriched in mouse m576, representing, respectively, 0.01% and 11.43% of the population in the primary tumor and its surgical bed. Notably, although never dominating in any of the eight recurrent tumors previously analyzed, R10 was identified in 5 of 7 tumor beds and was thus the most common clone in surgical beds (Figures 3F and 3G). Mirroring the clonal substitution observed between primary and recurrent tumors, the first-ranked clone in each tumor bed was always different from the first-ranked clone in the matched primary tumor (Figure 3H). Although this analysis has confirmed the enrichment of some clones, it very likely underestimates the total complexity of the disseminated population, as clones located beyond the analyzed muscular layer may be missed. In summary, multiple clones remain after surgery in the tumor beds and potentially compete in the MRD for regrowth.

Recurrence-Initiating and Invasive Properties of Clones Dominating in Recurrent Tumors

To test whether the ability to initiate recurrence is preserved in recurrence-derived explants, we reimplanted the explants in mice. All but one explant demonstrated an increased tumor growth rate (especially 407R) and a quicker onset of postsurgical

(D) For each mouse, the proportion of hues shown in (C) (and also in Figure S2C) specific for primar7y tumors (green), recurrent tumors (magenta), or shared between matched tumors (black) is indicated as a percentage of the total number of hues.
(E) Lyve-1 immunofluorescence staining in an RGB32 primary tumor showing lymphovascular invasion (LVI) just outside of the primary tumor mass. The arrowhead indicates Lyve-1 positive lymphatic vessels.
(F) Further examples of Lyve-1 immunofluorescence staining showing instances of intratumoral LVI. Arrowheads indicate Lyve-1 positively lymphatic vessels.
(G) Representative image from a primary tumor showing a more uniform color in the peritumoral area compared to the more heterogeneous intratumoral area (also evident in E).

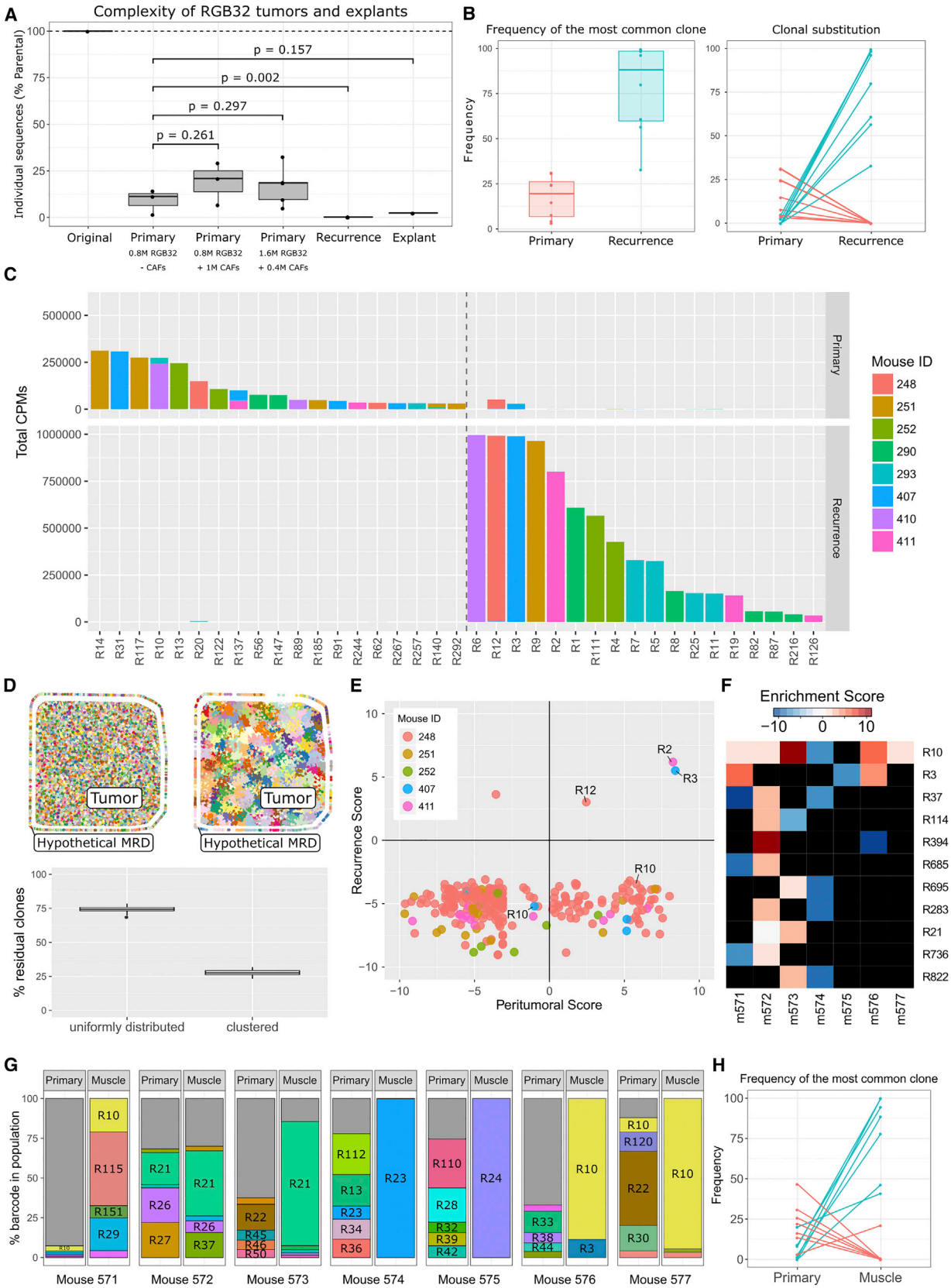

(legend on next page)

recurrences when compared to parental RGB32 cells (Figure 4A). In addition to R3 (from explant 407R), recurrence-initiating capacity was also confirmed for R2 and R19 (both constituting explant 411R) as well as R7 (from explant 293R), while other abundant clones in explant 293R (R5/R11/R25) failed to initiate second-generation recurrences (Figure 4B). These data indicate that recurrence-initiating capacity is limited to few clones and greatly varies between competitive clones, suggesting that some clones identified in recurrences could be ''passenger'' ones. Other less abundant ''passenger'' clones remained scarce in the reimplanted tumors and with few exceptions went completely undetected in second-generation recurrences (Figure 4B; Table S1). The most aggressive phenotype was observed for explant 407R (enriched in R3), which was not only quickly growing as a new primary tumor, but was also able to initiate a multinodular, highly invasive recurrence metastasizing into the neck lymph node (Figure 4C). Furthermore, explant 407R demonstrated prominent invasive behavior in organotypic co-cultures with immortalized CAFs (Figures S4A–S4D). Compared to RGB32 cells, admixing of explant 407R with CAL27 (at ratio 1:4) thickened the organotype's invasive layer at the expense of the basal layer (Figures S4A and S4B). In addition, whereas RGB32 cells were present throughout all layers and slightly enriched in the differentiated layer, 407R cells were almost exclusively restricted to the invasive layer (Figures S4C–S4D), illustrating a stronger invasive potential of these cells compared to the heterogeneous parental population. Thus, the recurrence-initiating potential seen in a limited number of clones (RTICs) was very likely related to their unique ability to acquire an invasive phenotype.

Progressing EMT in RTICs

To investigate the invasion-related properties of RTICs, we focused on EMT. Expression of vimentin, a mesenchymal marker, by a fraction of cancer cells in primary and recurrent tumors (Figures S4E and S4F) indicates that these cells were able to undergo EMT. The EMT phenotype clearly progressed between the first and second generations of explants (after reimplantation), as evident by a significant increase in expression of the EMT transcription factors *ZEB1* and *SNAI2* (Figure 4D) and by a progressive loss of E-cadherin (Figure 4E) in second-generation explants. Furthermore, when compared to parental RGB32 cells or to the first-generation explant 293R, both SLUG (*SNAI2* product) and ZEB1 proteins accumulate in the nuclei of the second-generation explant 578R (Figures S4G and S4H). We reasoned that the EMT phenotype of RTICs might represent a promising therapy target. Indeed, we found improved recurrence-free survival of CAL27 tumor-bearing mice treated with a combination of neo-adjuvant and adjuvant administration of the c-MET/ALK inhibitor crizotinib (Figure S4I), an observation deserving further investigations.

Expression of Cell-Surface Protein CD10 Is Shared by Some TICs and RTICs

To identify potential markers of RTICs and prospective targets for therapy, we performed membrane-enriched proteomics analysis (Zougman et al., 2014) using parental cell lines and recurrence-derived explants. Remarkably, 407R cell line distinctively expressed membrane-associated MME (CD10) as well as higher levels of EGFR protein, which was constitutively phosphorylated on residue Y1068 in a serum-independent fashion (Figure 5A). CD10 is a CSC marker in HNSCC (Fukusumi et al., 2014) and hence is a good candidate marker for RTICs. We anticipated that cell-surface expression of CD10 in 407R cells (enriched for R3 RTIC) could be used in combination with R3 intrinsic color to isolate this clone from the RGB32 population (Figure 5B). Indeed, R3 (5.1%) as well as other RTICs (such as R2 and R19) and unexpectedly also R10 (8.9%; defined as tumor-initiating clone, TIC, because of its observed relative prevalence in primary tumors) (Figures 3C and 3G) were detected in the sorted $CD10^{high}$ fraction of RGB32 cells (Table S1). Surprisingly, R2, R3 and R19 clones vanished after *in vitro* culture of both $CD10^{high}$ and $CD10^{high}/PE^{high}$ subpopulations, whereas R10 remained as the most abundant clone (2.4% and 21.6%; Table S1). Tumors established by cultured $CD10^{high}$ subpopulation grew faster as compared to $CD10^{low}$ subpopulation (Figure 5C) and were dominated by R10 (between 35.5% and 77.2%; Figure 5D; Table S1). In two mice from the $CD10^{high}$

Figure 3. Clonal Substitution in Recurrent HNSCC Tumors

(A) Clonal complexity of primary tumors with (n = 7) or without (n = 3) co-implantation of CAFs, recurrent tumors (n = 8) and recurrence-derived explant cell lines (n = 3). Boxplots indicate the relative numbers of individual barcodes identified in each sample compared to the total number of individual barcodes of the reference RGB32 cell line after normalizing to the sequencing depth of each corresponding library. p, p value.

(B) The cellular contribution of the most abundant clones to the bulk of barcodes of each tumor is indicated by a boxplot (left panel). The frequency of these most abundant clones in matching primary and recurrent tumors illustrates a clonal substitution (right panel).

(C) Bars indicate barcodes with total counts per million (CPMs) of at least 30,000 across samples. The top panel indicates the clonal distribution in primary tumors, and the bottom panel depicts clonal distribution in recurrent tumors (see also Figures S3A–S3H). Individual mice are color-coded.

(D) Schematic illustration of two different scenarios for spatial clonal distributions. The top-left setting contains a spatially uniform distribution of cells from 400 representative clones, and cells from the same clones are spatially confined in the top-right scenario. Considering the abundance of clones in the MRD that represent 1% of the total area, the boxplots quantify the level of clonal diversity in the MRD over 100 simulations, which is reduced for the scenario with spatially confined clones.

(E) Scatterplot highlighting the correlation between the enrichment of clones at the tumor periphery (peritumoral score) and their enrichment in recurrent tumors (recurrence score). R2, R3, and R12 represent RTICs enriched at the tumor periphery and in recurrences.

(F) Heatmap showing all clones able to disseminate in the muscle of at least two animals, with a positive enrichment score for at least one of them. The black cells in the heatmap correspond to missing values (meaning that the barcode was not found in this sample, neither in the tumor nor in the surgical bed).

(G) Bars indicate the relative frequency of the top-five clones in each matched primary tumor and muscle. For each mouse, different barcodes are shown by different colors and the most abundant barcodes are explicitly labeled. The sum of all barcodes that are ranked below the top-five most abundant clones is depicted in gray.

(H) The frequency of the most abundant clones in matching primary tumors and tumor beds illustrates a clonal substitution.

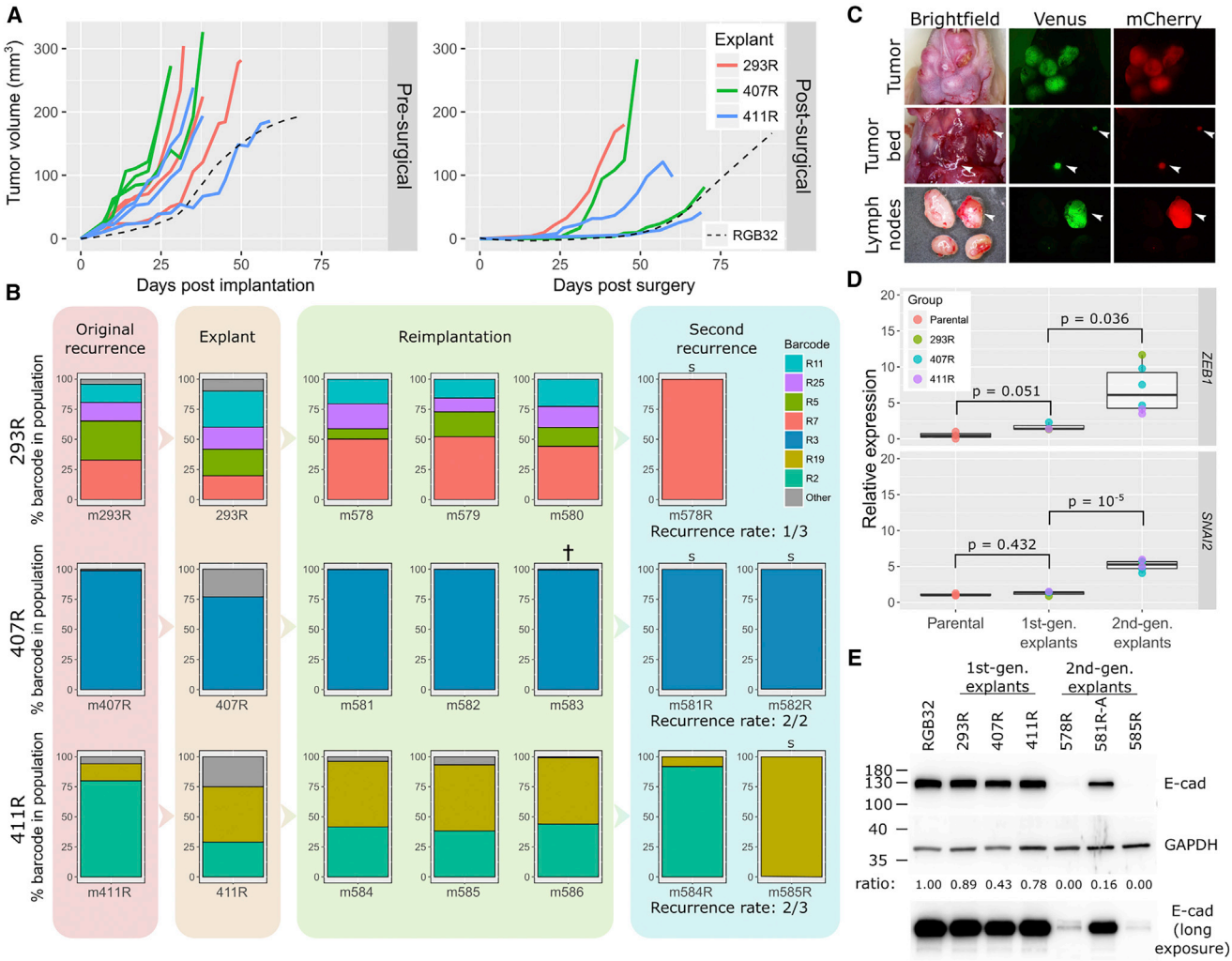

Figure 4. Selection of Pro-EMT Features and Aggressive Phenotype by Reimplantation of Recurrence-Derived Explant Cell Lines

(A) Tumor growth curves following reimplantation of recurrence-derived explant cell lines as compared to mice injected with the parental RGB32 cell line. The dashed lines indicate the average growth (by loess regression) of RGB32 tumors reported in Figure 1B.

(B) Clonal evolution of recurrence-derived explant cell lines following reimplantation in mice. The contribution of clones dominating in the original recurrence and explants (left) is largely maintained in the newly developing tumors of three independent mice per explant cell line (middle). The rate of recurrence (second-generation recurrence) following surgery is indicated for each explant (right). One mouse was sacrificed before surgery (†). Where possible (expected monoclonal sample), NGS was substituted by Sanger sequencing (S).

(C) Fluorescence imaging of an aggressive recurrence (407R/m581) with multinodular growth, deep invasion in tissue and LN metastasis.

(D) qRT-PCR expression profiles for the EMT markers *ZEB1* and *SNAI2* in a series of parental cells (CAL27, CRGB, RGB32), first-generation explants (293R, 407R, 411R), and second-generation recurrence explants (derived in B, n = 6 explants). p, p value.

(E) Immunoblot analysis of E-cadherin in the original RGB32 cell line and first- and second-generation recurrence explants (derived in B). Relative E-cadherin signal (relative to GAPDH) was calculated and is indicated below. In addition, a longer exposure for E-cadherin is presented at the bottom.

See also Figure S4.

group, R10 quasi-monoclonal recurrences (tumor and LN metastasis) and one additional polyclonal, R10-poor (0.3%) recurrent tumor developed after surgery. Single-clone enriched recurrences also developed in two mice with $CD10^{low}$ tumors, showing clonal substitution in m669 mouse but regrowth of the dominant clone in m670 mouse. Taken together, expression of a common marker, i.e., CD10, between a subset of TICs (represented by R10) and RTICs indicates that they may have a common origin, and thus share the proficiency to initiate post-surgical recurrences. However, this recurrence-initiating aptitude seemed regulated by external factors such as the overall cellular complexity.

RTICs Show Private and Shared Genetic Features

To find out whether the recurrence-initiating capacity is related to a certain genetic profile, we performed exome-seq analysis of parental (n = 3) and explant cell lines of the first- (n = 3) and second-generation (n = 9) recurrent tumors. These explants included

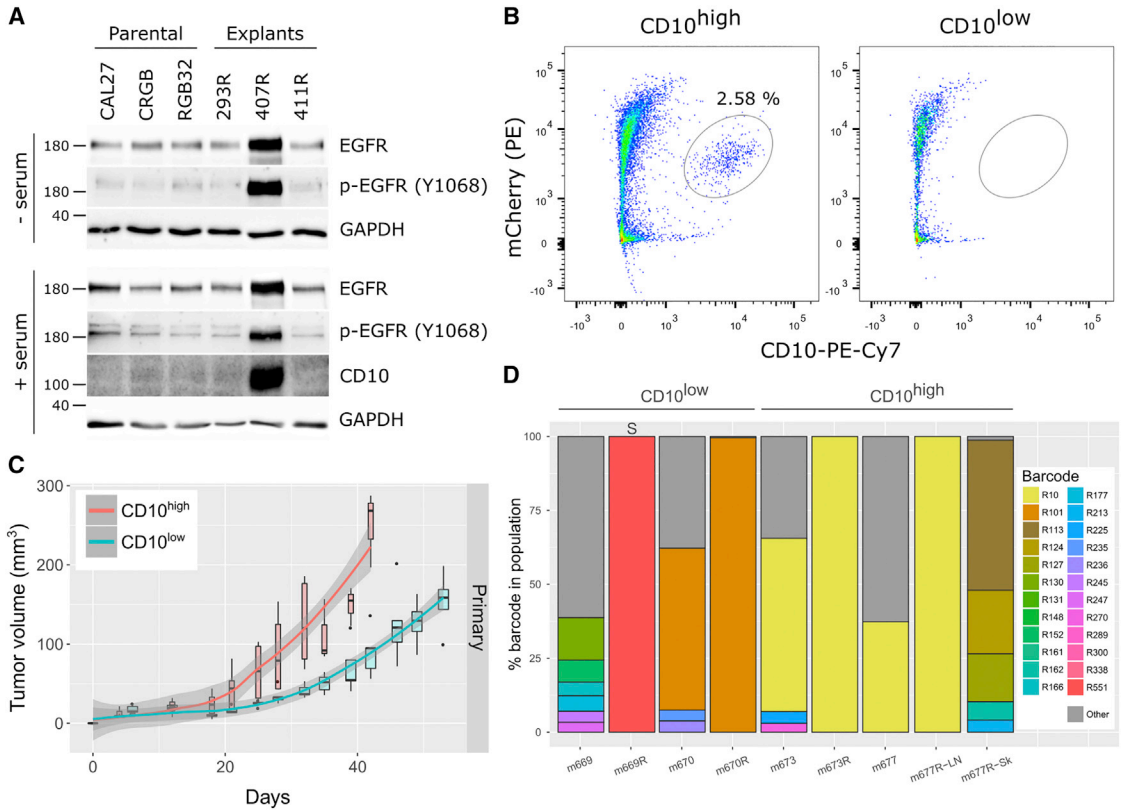

Figure 5. CD10 as a Marker of Cells with Tumor-Initiating Potential

(A) Immunoblot analysis demonstrating CD10 and EGFR overexpression as well as EGFR autoactivation in explant 407R as compared to parental cell lines and other explants.

(B) Fluorescence-activated cell sorting (FACS) analysis of $CD10^{high}$ sorted cells before *in vivo* implantation. Despite some plasticity, a significant fraction of cells retained high expression of CD10.

(C) Growth curve of primary tumors following implantation of $CD10^{high}$ or $CD10^{low}$ cells showing acceleration of the growth kinetics in mice implanted with $CD10^{high}$ cells.

(D) Clonal distribution in mice implanted with $CD10^{high}$ or $CD10^{low}$ cells. Bars indicate the relative frequency of clones in corresponding primary and recurrent (R) tumors. For each mouse, different barcodes are shown by different colors. S, analyzed by Sanger sequencing. LN, recurrence located in the neck lymph node area. Sk, recurrence located in the neck skin.

quasi-monoclonal RTICs (R2, R3, R7, and R19) and the quasi-monoclonal R10 TIC. Our CAL27 stock and its two subsequent derivatives (CRGB and RGB32) showed concordance in 52 of 54 CAL27-specific SNPs retrieved from the CCLE database, confirming relatively high genomic stability in our cell lines (Figure S5A). The genomic landscape of each explant is presented in Figure 6. When compared to RGB32, most explants were characterized by a modest change in the alternate allele frequency (AF) of the identified variants (Table S2; single-nucleotide variations [SNVs]; Figure 6A), while explants enriched in R3 showed extensive allelic variations, segregating this clone from the parental population. However, more than half of the CAL27 specific SNPs, including those in *TP53* and *TGFBR1* genes, were preserved and hence confirmed the shared clonal origin of R3 and the rest of the parental population (Figure S5A). Few private (e.g., *PRKG2* R282T in R19) or shared (e.g., *RNF123* M1087I in R2 and R7) variants were identified for a series of RTICs (Figure 6A). In addition, private heteroplasmic variants were found in mitochondrial DNA (mtDNA) of RTICs, such as C114T and G225T (both in D-loop region) in R3 and R7, respectively, and *MT-ND1* C3946T (E214*) shared mutation in R2, R7, and R19 (Table S2).

On a chromosomal level, explant cell lines showed both shared and private gains and losses of focal or sub-chromosomal nature (Table S3; copy number variations [CNVs]; Figure 6B). Interestingly, a regional gain on chromosome 20p, which contains *PCNA* gene (among others), was shared between four RTICs (R2, R3, R7, and R19) (Figure 6B). An additional allele of *PCNA* gene could theoretically confer a proliferative advantage to RTICs during their outgrowth from MRD. In addition, a region including the known tumor suppressor gene *MYH9* (on chromosome 22) (Schramek et al., 2014) was lost in R19 (Figure 6B).

Remarkably, second-generation explants either derived by *in vitro* culture or *in vivo* growth showed a minimal number of novel mutations and aberrations compared to first-generation explants, even in the case of the explant derived from a LN metastasis. In particular, R19 enriched either by cell sorting ($411R/Ve^{lo}$) or in the second-generation explants (585R) showed highly concordant genetic profiles (Figure 6A). Indeed, only five

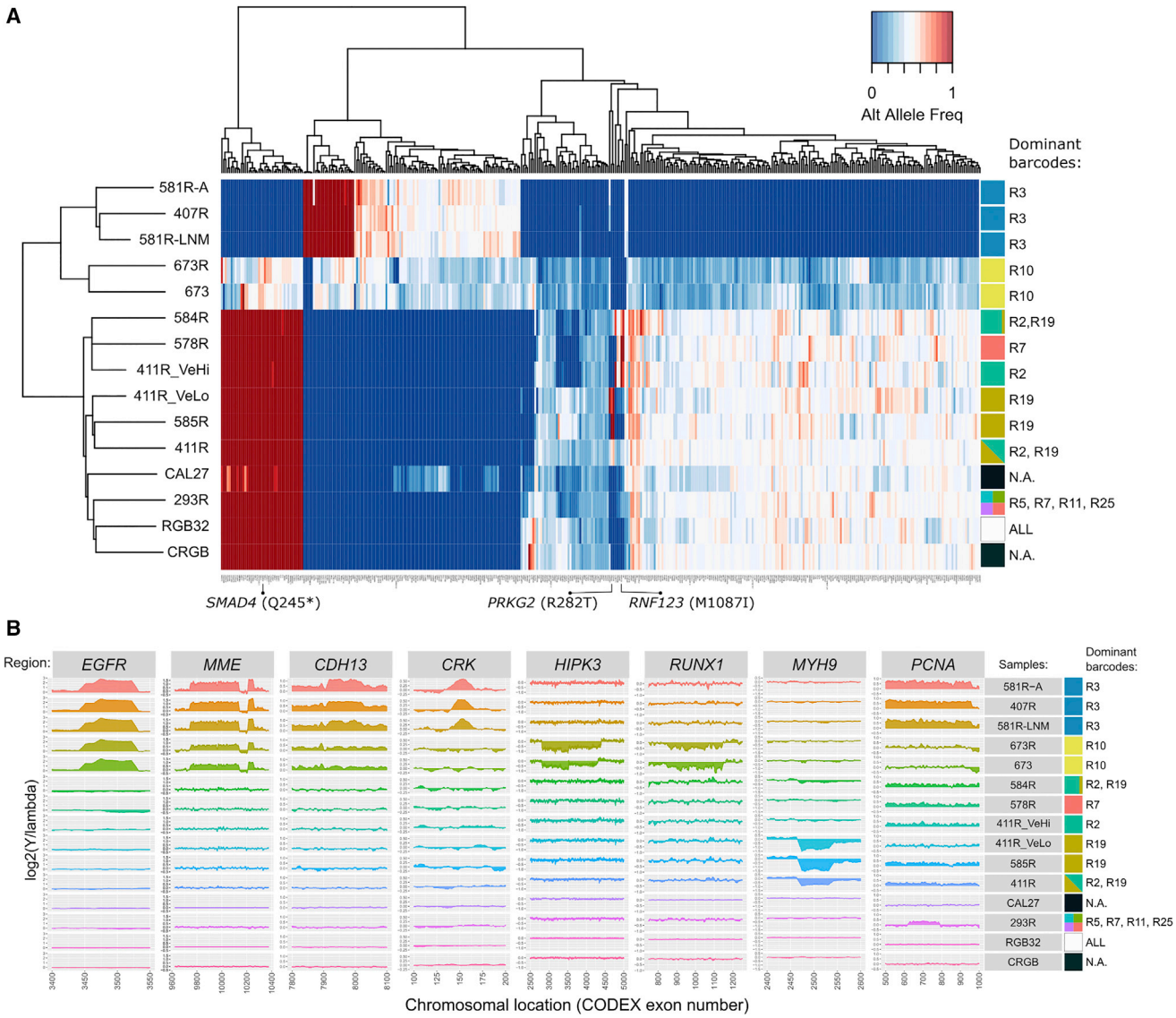

Figure 6. Characterization of Recurrence-Derived Explants by Whole-Exome Sequencing

(A) Heatmap comparing the alternate AF of all SNPs identified in reference (CAL27, CRGB, and RGB32) and explant cell lines. Explant names are indicated on the left side of the heatmap, and major barcodes constituting these explants are indicated on the right. Heterozygous (for R10) or homozygous (for R3) wild-typing of the *SMAD4* Q245* variant and private mutations for other clones are indicated at the bottom.

(B) CNV analysis across the explant cell lines calculated using CODEX R package following exome sequencing. Each column shows a representative private or shared regional DNA alteration. The y axis represents the copy number and is approximated by the logarithmic ratio of CODEX normalized counts divided by raw counts.

See also Figure S5.

novel variants were detected (all at a frequency below 0.31) in explant 585R when compared to the sorted 411R/Ve^{lo} explant (Table S2). Similarly, only eight novel variants were detected (all at a frequency below 0.16) when comparing R3 detected in the first- (407R) and second-generation explants (581R-A and 581R-LNM) (Table S2).

R3 and R10 Clones Belong to the Same Lineage

Beyond the fact that R3 and R10 express CD10, there was a gradual increase in the absolute allelic distance (i.e., the difference in alternate AF between a subject and its reference) from the parental RGB32 cell line to R10 explants and to R3 explants. In particular, R3 was featured by complete wild-typing of *SMAD4* Q245* mutation, whereas R10 was heterozygous for this variant (Figure 6A). Consistently, while SMAD4 was undetectable in CAL27 parental population, its expression was restored in explants enriched in R3 and R10 or in sorted CD10^{high} cells (Figure S5B). Notably, reconstitution of SMAD4 was not sufficient to convey TGF-β pathway signaling (Figure S5C), hence indicating a non-canonical function of SMAD4. CD10 and EGFR

were also prominently expressed by R10 and CD10^{high} cells (Figure S5B), further supporting the likelihood of a common ancestor for R10 and R3 in the CAL27 population. Thus, we reason that such ancestor clone bearing *SMAD4* wild-type (WT) allele persists in CAL27 cell culture, and we suspect that R10 precedes R3 in the clonal evolution. This hypothesis is further supported by (1) a progressing gain in regions encompassing *EGFR* (chromosome 7) and *MME* (chromosome 3) genes in R10 and R3 as compared to RGB32 cells (Figure 6B), (2) an increasing wild-type frequency of nonsynonymous mutations in genes located in a 45-Mb region on chromosome 4, a 54-Mb region on chromosome 5 and a 43-Mb region on chromosome 8 in R10 and R3 as compared to RGB32 cells (Figure S5D), and (3) the presence of a heteroplasmic C114T variant in mtDNA of R3, but not R10 (Table S2). Furthermore, a set of private variants supports a divergent evolution of R3 and R10 from a common ancestor: while gains encompassing *CDH13* (chromosome 16) and *CRK* genes (chromosome 17) were found in R3, losses including *HIPK3* (chromosome 11) and *RUNX1* (chromosome 21) genes were characteristic for R10 (Figure 6B). Altogether, the genetic analysis of R3 and R10 clones indicates that tumor-initiating clones with different potential to outgrow in recurrences may arise during tumor evolution from common, genetically unique ancestors that substantially differ from other subclonal lineages.

DISCUSSION

Permanent cell marking has become an extremely useful tool to study clonal dynamics (Blundell and Levy, 2014). In the present study, we further advanced the joint application of RGB marking and DNA barcoding (Cornils et al., 2014) for clonal tracking by two modifications. First, based on the separation of RGB and barcoding vectors we ensured the presence of unique barcodes in single marked cells. Second, we exploited an improved BC32 barcode running on a high level of complexity, thus limiting the systematic bias inherent to previous techniques (Thielecke et al., 2017) and making it the appropriate tool to perform clonal deconvolution in highly heterogeneous cancer cell populations.

Using cellular barcoding, we provide a comprehensive clonal analysis of matched primary and recurrent tumors in a surgical mouse model of HNSCC, and we highlight a distinct nature of clones prevailing in postsurgical local recurrences. Initially, these clones successfully propagated into the adjacent tissue remaining after surgery, which can be viewed as a potential niche hosting the residual malignant cells. These cells constituting the MRD are clinically undetectable by conventional intraoperative microscopic evaluation. In HNSCC patients, even though both mucosal and deep surgical margins may prove free of malignant cells microscopically, the risk of recurrences is particularly increased with detection of tumor-specific *TP53* mutations in the margin tissue (Brennan et al., 1995; Pena Murillo et al., 2012). This, together with predominant correspondence of *TP53* mutations between primary HNSCC tumors and matched recurrences (Hedberg et al., 2016; van Ginkel et al., 2016), suggests that the latter may originate from pre-existing, invasive lineages. These stem-like malignant cells could be endowed not only with high invasive potential but also competency to repopulate tumors starting from few residual cells. Our data support this concept by providing evidence that a limited number of clones spread and undergo further selection resulting in the outgrowth of recurrences with a greatly reduced clonal diversity.

Although many aspects of clonal identity and dynamics, in particular mechanisms of clonal interactions, migratory activity and fitness within a complex milieu of invasively growing HNSCC tumors and postsurgical MRD remain to be elucidated, we attempted to summarize our current understanding of postsurgical progression in HNSCC as a hypothetical model (Figure 7). In this model, the co-occurrence of neutral and non-neutral mechanisms of selection taking place in concert in the MRD could be a rational explanation for the phenotype of clonal substitution observed in our data. Based on their ability to initiate well-differentiated squamous primary and recurrent tumors, we defined clones that prevailed in individual primary tumors as TICs and clones that substantially contributed to the postsurgical recurrences as RTICs. The remaining sparse clones in primary tumors (defined as non-TICs) vanished during tumor growth probably going from a transient proliferation state to a terminal squamous differentiation state. Such categorization of clones is not necessarily restricted to a pre-existing segregation into respective branches, but may possibly have a conditional nature, as it is expectedly influenced by the overall clonal complexity, i.e., by the magnitude of interclonal interactions and competition during tumor growth and by specific signals produced by the tumor microenvironment. Dominance of certain clones in the recurrences could be potentially attributed, as our results suggest, to special genetic traits. However, such dominance also can be possibly caused by a conditionally enhanced ability to seed around the tumor by migratory activity or lymphatic dissemination.

We hypothesize that clones that reached the tumor periphery either by directed migration or by chance (e.g., as accidental followers of migrating leader cells or due to a fortuitous location during tumor growth) might compete for growth and experience unbalanced proliferative activity resulting in clones of unequal sizes at the tumor edges. Thus, the incidence of peritumoral seeding could be biased toward more abundant clones located at the tumor front. This could be true, if clones enriched at the front are equipotent to spread. However, the ability to spread by invasion may differ within peripheral clones and thus be the most critical prerequisite for a clone at the tumor edge to eventually contribute to the outgrowth of tumor after surgery. Invasive cells settled around the tumor and remaining after surgery may resume growth and generate nests of either spatially linked or separated clones, which can further undergo either neutral or directed selection for one or few winner clones, which are the fittest to establish recurrent tumors. Such interclonal interactions may include both (1) competition between clones with different potential to grow under conditions that differ from what they experienced in primary tumor and (2) non-selective regrowth of one or few clones at the expense of other functionally equal clones. Any clone that managed to contribute to the initial stage of residual disease (i.e., peritumoral seeding followed by resumed proliferation) may not necessarily vanish as a consequence of competitive interactions, but can remain as low-abundant passenger with a negligible contribution to the postsurgical

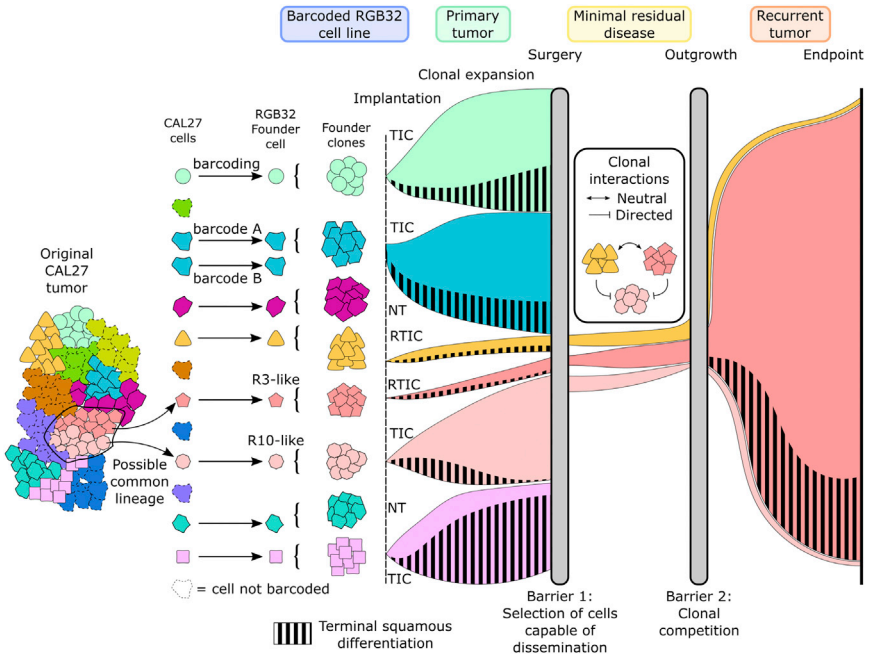

Figure 7. Proposed Clonal Model

All CAL27 cells in the original human tumor are anticipated to be of clonal origin and share a number of clonal mutations (e.g., in *TP53*). Within the tumor, different subclonal populations defined by additional genetic alterations coexist and some of them might come from a common lineage. Cellular barcoding then results in a series of clonally expanded *founder cells*. Depending on the heterogeneity of the tested cell population at the time of transduction, the barcoding step in principle *might* result in the labeling of several identical, i.e., clonally derived, cells with different barcodes (barcode A, barcode B), though the resultant barcoded cells will at least differ by their respective viral integration sites. After implantation of barcoded *founder clones* in mice, tumors showed enrichment for a few proliferating clones (TICs) and a very low frequency of one or few clones that became dominant after regrowth from the MRD (RTICs), while most of the *founder clones* were not tumorigenic (non-TIC, NT). Cells contributing to recurrences need to overcome two barriers. First, they must leave the tumor mass and disseminate in the MRD to escape from the extensive surgical resection. Next, TICs and RTICs are likely subjected to both neutral and directed clonal interactions in the MRD. Whereas directed selection could potentially prevent TICs from growing out of the MRD, the selection of RTICs that ultimately dominate in the recurrences could be the result of neutral selection between clones with equal recurrence-promoting potential. Tumors developing from both TICs and RTICs have the ability to commit various numbers of cells to terminal squamous differentiation (shaded areas).

recurrence. However, such clones may potentially contribute to the clonal evolution of the tumor, if adjuvant therapy (e.g., chemoradiation) follows the surgery.

It is tempting to speculate that tumor microenvironment, in particular via the supply of cancer cells with hepatocyte growth factor (HGF) (Knowles et al., 2009), epidermal growth factor (EGF) (Zhang et al., 2014), or transforming growth factor β (TGF-β) (Oshimori et al., 2015) could possibly change the clonal landscape of the invasively growing tumor, influence the phenotype of clonal populations at the tumor front and confer survival benefit to residual cells. In particular, stromal factors may induce some phenotypic plasticity in cancer cells, including acquisition of EMT traits. It was shown that EMT in HNSCC, like in other carcinomas, could be, in particular, induced by HGF provided by fibroblasts in the tumor stroma (Knowles et al., 2009) or hypoxia (Gammon and Mackenzie, 2016), a condition that residual cells may experience at their niches. After surgery, residual cells will be exposed to tissue-remodeling factors released during postsurgical wound healing, known to promote tumor growth and metastasis (Ceelen et al., 2014). The combination of wound-associated factors, in particular EGF-like factors that stimulate the proliferation of EGFR-overexpressing HNSCC cells (Licitra et al., 2011) and the inherent ability of residual clones to compete for survival within this environment, could collectively select for the fittest clone(s) with tumor-initiating potential.

Genetic analysis indicates that clones massively enriched in postsurgical recurrences could represent lineages that emerged either independently during tumor evolution or that originated from a very early ancestor, whose progeny may share many common features, such as stemness and invasiveness. For example, in the parental CAL27 population, cells featured by wild-type alleles of *SMAD4* gene very likely originated from an early ancestor heterozygous for *SMAD4* mutation (represented by clone R10), from which numerous descendants evolved toward homozygosity of mutant *SMAD4* allele, whereas a small fraction of daughter cells preserved the wild-type allele (represented by clone R3). Such separation between ancestral branches and their progeny could possibly have resulted from chromosomal segregation errors causing asymmetric distribution of wild-type and mutant alleles. Chromosomal rearrangements known to accompany tumor progression by fueling cancer evolution and adaptation (Sansregret and Swanton, 2017) may eventually cause the emergence of genetic variants with a higher potential to seed and establish recurrences after resection of highly heterogeneous tumors.

Although our barcoding technology unambiguously revealed clonal substitution after resection of RGB32 tumors, previous reports inferring clonality from variant allele frequencies in patient samples showed a similar succession of dominant lineages in recurrent cancers, such as acute myeloid leukemia (Ding et al., 2012), T cell acute lymphoblastic leukemia (Kunz et al., 2015), breast cancer (Hoadley et al., 2016), and glioma (Johnson et al., 2014). In addition, rare pre-existing clones selected by surgery and radiotherapy were identified in a mouse model of recurrent medulloblastoma (Morrissy et al., 2016). Although potential adjuvant therapy would also contribute to clonal substitution in recurrent tumors, we clearly show that surgery alone results in a more homogeneous, sometimes nearly monoclonal postsurgical recurrence, as compared to the primary tumor.

Consequently, personalized therapies targeting such clonal populations might be developed into a successful treatment approach in the future. In this context, the identification of EMT as one of the common pathways exploited by clones enriched in recurrent tumors provides a rationale for pharmacological interventions. The reduced incidence of postsurgical recurrences in the CAL27 model after treatment with crizotinib strongly supports the pivotal role of EMT, at least EMT initiated via c-MET, in the outgrowth of recurrent tumors and exemplifies a possible strategy to prevent recurrences.

Although our mouse model is unrivaled for the tracking of clonal populations contributing to tumor regrowth after surgery and testing of specific targeting approaches, it is limited by the low rate of LN metastasis and the absence of distant metastatic disease, representing other typical features of HNSCC. Despite these shortcomings, our work serves to build a working model explaining clonal events after surgery and as a proof of technology, which can be transferred to other surgical models of HNSCC for clonal tracking of LN and distant metastasis. In conclusion, we believe that the systematic study of clonal events implicated in the development of recurrences after surgery will greatly facilitate the establishment of therapies urgently needed to improve survival of HNSCC patients.

STAR★METHODS

Detailed methods are provided in the online version of this paper and include the following:

- KEY RESOURCES TABLE
- CONTACT FOR REAGENT AND RESOURCE SHARING
- EXPERIMENTAL MODEL AND SUBJECT DETAILS
  - Mice
  - Cell culture and generation of cell lines
- METHOD DETAILS
  - Generation of barcoded cells (see also Figure S6A)
  - Generation of explant cell lines (see also Figure S6A)
  - Generation of cell lines by cell sorting
  - Cell culture of CAFs
  - Organotypic cell culture
  - Surgical mouse model of HNSCC tumors
  - Crizotinib treatment of tumor-bearing animals
  - Histology and Immunofluorescence
  - DNA extraction and BC32 barcode retrieval
  - Laser microdissection
  - RNA isolation and RT-qPCR
  - Immunoblotting
  - Sanger sequencing
  - Analysis of BC32 barcode sequences (Bar-Seq)
  - Fluorescence imaging and spectral analysis
  - Exome **sequencing, variants and copy** number variation analysis
  - Membrane proteomics
- QUANTIFICATION AND STATISTICAL ANALYSIS
  - Mathematical methods
  - Statistics
- DATA AND SOFTWARE AVAILABILITY

SUPPLEMENTAL INFORMATION

Supplemental Information includes six figures and three tables and can be found with this article online at https://doi.org/10.1016/j.celrep.2018.10.090.

ACKNOWLEDGMENTS

This work is dedicated to the memory of Dr. Richard Latsis, our teacher and friend. We thank institutional facilities, especially the Biopole's Animal Facility and their caretakers, Vital-IT (Swiss Institute of Bioinformatics), the FACS Core Facility (M. Lachmann and S. Roscher) at UKE, and the Genomics & Proteomics Core Facility of the DKFZ (Heidelberg). We also thank K. Riecken (UKE) and R. Genolet (UNIL) for their kind support with the LeGO vector technology and Bar-Seq, respectively. This work was supported by DACH-DFG/SNF (310030L_144267 to C.S.; AB 338/5-1 to A.A.), SNF (310030_152875 to G.V.T.), the Faculty of Biology and Medicine of UNIL (to C.S.), Krebsliga Schweiz (KLS-3853-02-2016-R to Y.M. and G.V.T.), the Fondation pour la lutte contre le cancer (to G.V.T.), Novartis Foundation for Medical Biological Research (13C131 to G.V.T.), HGF-iMED and National Center for Tumor Diseases (NCT3.0_2015.21 NCT-PRO to A.A.), Forschungs und Wissenschaftsstiftung Hamburg within LExI (to B.F.), Deutsche Krebshilfe (110619 to K.C., I.G., and B.F.; 111303 to B.F.), DFG (FE568/11-2 to B.F.; CO 1692/1-1 and GL 721/1-1 to K.C., I.G., and L.T.), and BMBF (031A315 "MessAge" to I.G.).

AUTHOR CONTRIBUTIONS

Conceptualization, C.S., A.A., and G.V.T.; Methodology, P.A., K.C., T.A., B.F., C.S., and G.V.T.; Software, V.R.; Formal Analysis, V.R.; Investigation, V.R., P.A., A.H.-F., K.C., J.-P.R., A.Z., L.T., Z.T., M.M., A.N., and I.G.; Resources, A.Z., Y.M., I.G., V.P., A.A., K.C., B.F., C.S., and G.V.T.; Writing – Original Draft, V.R. and G.V.T.; Writing – Review & Editing, V.R., P.A., K.C., I.G., B.F., C.S., and G.V.T.; Supervision, C.S. and G.V.T.; and Funding Acquisition, K.C., B.F., C.S., and G.V.T.

DECLARATION OF INTERESTS

The authors declare no competing interests.

Received: May 25, 2017
Revised: September 4, 2018
Accepted: October 24, 2018
Published: November 20, 2018

REFERENCES

Behren, A., Kamenisch, Y., Muehlen, S., Flechtenmacher, C., Haberkorn, U., Hilber, H., Myers, J.N., Bergmann, Z., Plinkert, P.K., and Simon, C. (2010). Development of an oral cancer recurrence mouse model after surgical resection. Int. J. Oncol. *36*, 849–855.

Blundell, J.R., and Levy, S.F. (2014). Beyond genome sequencing: lineage tracking with barcodes to study the dynamics of evolution, infection, and cancer. Genomics *104* (*6 Pt A*), 417–430.

Brennan, J.A., Mao, L., Hruban, R.H., Boyle, J.O., Eby, Y.J., Koch, W.M., Goodman, S.N., and Sidransky, D. (1995). Molecular assessment of histopathological staging in squamous-cell carcinoma of the head and neck. N. Engl. J. Med. *332*, 429–435.

Ceelen, W., Pattyn, P., and Mareel, M. (2014). Surgery, wound healing, and metastasis: recent insights and clinical implications. Crit. Rev. Oncol. Hematol. *89*, 16–26.

Celià-Terrassa, T., and Kang, Y. (2016). Distinctive properties of metastasis-initiating cells. Genes Dev. *30*, 892–908.

Cheung, K.J., and Ewald, A.J. (2016). A collective route to metastasis: seeding by tumor cell clusters. Science *352*, 167–169.

Cornils, K., Thielecke, L., Hüser, S., Forgber, M., Thomaschewski, M., Kleist, N., Hussein, K., Riecken, K., Volz, T., Gerdes, S., et al. (2014). Multiplexing

clonality: combining RGB marking and genetic barcoding. Nucleic Acids Res. *42*, e56.

Ding, L., Ley, T.J., Larson, D.E., Miller, C.A., Koboldt, D.C., Welch, J.S., Ritchey, J.K., Young, M.A., Lamprecht, T., McLellan, M.D., et al. (2012). Clonal evolution in relapsed acute myeloid leukaemia revealed by whole-genome sequencing. Nature *481*, 506–510.

Fehse, B., Kustikova, O.S., Bubenheim, M., and Baum, C. (2004). Pois(s)on–it's a question of dose. Gene Ther. *11*, 879–881.

Fukusumi, T., Ishii, H., Konno, M., Yasui, T., Nakahara, S., Takenaka, Y., Yamamoto, Y., Nishikawa, S., Kano, Y., Ogawa, H., et al. (2014). CD10 as a novel marker of therapeutic resistance and cancer stem cells in head and neck squamous cell carcinoma. Br. J. Cancer *111*, 506–514.

Gammon, L., and Mackenzie, I.C. (2016). Roles of hypoxia, stem cells and epithelial-mesenchymal transition in the spread and treatment resistance of head and neck cancer. J. Oral Pathol. Med. *45*, 77–82.

Gath, H.J., and Brakenhoff, R.H. (1999). Minimal residual disease in head and neck cancer. Cancer Metastasis Rev. *18*, 109–126.

Gleber-Netto, F.O., Braakhuis, B.J., Triantafyllou, A., Takes, R.P., Kelner, N., Rodrigo, J.P., Strojan, P., Vander Poorten, V., Rapidis, A.D., Rinaldo, A., et al. (2015). Molecular events in relapsed oral squamous cell carcinoma: Recurrence vs. secondary primary tumor. Oral Oncol. *51*, 738–744.

Global Burden of Disease Cancer Collaboration; Fitzmaurice, C., Allen, C., Barber, R.M., Barregard, L., Bhutta, Z.A., Brenner, H., Dicker, D.J., Chimed-Orchir, O., Dandona, R., Dandona, L., et al. (2017). Global, regional, and national cancer incidence, mortality, years of life lost, years lived with disability, and disability-adjusted life-years for 32 cancer groups, 1990 to 2015: a systematic analysis for the global burden of disease study. JAMA Oncol. *3*, 524–548.

Hartig, R., Huang, Y., Janetzko, A., Shoeman, R., Grüb, S., and Traub, P. (1997). Binding of fluorescence- and gold-labeled oligodeoxyribonucleotides to cytoplasmic intermediate filaments in epithelial and fibroblast cells. Exp. Cell Res. *233*, 169–186.

Hedberg, M.L., Goh, G., Chiosea, S.I., Bauman, J.E., Freilino, M.L., Zeng, Y., Wang, L., Diergaarde, B.B., Gooding, W.E., Lui, V.W., et al. (2016). Genetic landscape of metastatic and recurrent head and neck squamous cell carcinoma. J. Clin. Invest. *126*, 169–180.

Hill, J.T., Demarest, B.L., Bisgrove, B.W., Su, Y.C., Smith, M., and Yost, H.J. (2014). Poly peak parser: Method and software for identification of unknown indels using sanger sequencing of polymerase chain reaction products. Dev. Dyn. *243*, 1632–1636.

Hoadley, K.A., Siegel, M.B., Kanchi, K.L., Miller, C.A., Ding, L., Zhao, W., He, X., Parker, J.S., Wendl, M.C., Fulton, R.S., et al. (2016). Tumor evolution in two patients with basal-like breast cancer: a retrospective genomics study of multiple metastases. PLoS Med. *13*, e1002174.

Jiang, Y., Oldridge, D.A., Diskin, S.J., and Zhang, N.R. (2015). CODEX: a normalization and copy number variation detection method for whole exome sequencing. Nucleic Acids Res. *43*, e39.

Johnson, B.E., Mazor, T., Hong, C., Barnes, M., Aihara, K., McLean, C.Y., Fouse, S.D., Yamamoto, S., Ueda, H., Tatsuno, K., et al. (2014). Mutational analysis reveals the origin and therapy-driven evolution of recurrent glioma. Science *343*, 189–193.

Knowles, L.M., Stabile, L.P., Egloff, A.M., Rothstein, M.E., Thomas, S.M., Gubish, C.T., Lerner, E.C., Seethala, R.R., Suzuki, S., Quesnelle, K.M., et al. (2009). HGF and c-Met participate in paracrine tumorigenic pathways in head and neck squamous cell cancer. Clin. Cancer Res. *15*, 3740–3750.

Kunz, J.B., Rausch, T., Bandapalli, O.R., Eilers, J., Pechanska, P., Schuessele, S., Assenov, Y., Stütz, A.M., Kirschner-Schwabe, R., Hof, J., et al. (2015). Pediatric T-cell lymphoblastic leukemia evolves into relapse by clonal selection, acquisition of mutations and promoter hypomethylation. Haematologica *100*, 1442–1450.

Kustikova, O.S., Wahlers, A., Kühlcke, K., Stahle, B., Zander, A.R., Baum, C., and Fehse, B. (2003). Dose finding with retroviral vectors: correlation of retroviral vector copy numbers in single cells with gene transfer efficiency in a cell population. Blood *102*, 3934–3937.

Lawrence, M., Huber, W., Pagès, H., Aboyoun, P., Carlson, M., Gentleman, R., Morgan, M.T., and Carey, V.J. (2013). Software for computing and annotating genomic ranges. PLoS Comput. Biol. *9*, e1003118.

Li, H., and Durbin, R. (2009). Fast and accurate short read alignment with Burrows-Wheeler transform. Bioinformatics *25*, 1754–1760.

Licitra, L., Perrone, F., Tamborini, E., Bertola, L., Ghirelli, C., Negri, T., Orsenigo, M., Filipazzi, P., Pastore, E., Pompilio, M., et al. (2011). Role of EGFR family receptors in proliferation of squamous carcinoma cells induced by wound healing fluids of head and neck cancer patients. Ann. Oncol. *22*, 1886–1893.

Liotta, L.A. (2016). Adhere, degrade, and move: the three-step model of invasion. Cancer Res. *76*, 3115–3117.

Marur, S., and Forastiere, A.A. (2016). Head and neck squamous cell carcinoma: update on epidemiology, diagnosis, and treatment. Mayo Clin. Proc. *91*, 386–396.

McGranahan, N., and Swanton, C. (2017). Clonal heterogeneity and tumor evolution: past, present, and the future. Cell *168*, 613–628.

Morgan, M., Anders, S., Lawrence, M., Aboyoun, P., Pagès, H., and Gentleman, R. (2009). ShortRead: a bioconductor package for input, quality assessment and exploration of high-throughput sequence data. Bioinformatics *25*, 2607–2608.

Morrissy, A.S., Garzia, L., Shih, D.J., Zuyderduyn, S., Huang, X., Skowron, P., Remke, M., Cavalli, F.M., Ramaswamy, V., Lindsay, P.E., et al. (2016). Divergent clonal selection dominates medulloblastoma at recurrence. Nature *529*, 351–357.

Obenchain, V., Lawrence, M., Carey, V., Gogarten, S., Shannon, P., and Morgan, M. (2014). VariantAnnotation: a Bioconductor package for exploration and annotation of genetic variants. Bioinformatics *30*, 2076–2078.

Oshimori, N., Oristian, D., and Fuchs, E. (2015). TGF-β promotes heterogeneity and drug resistance in squamous cell carcinoma. Cell *160*, 963–976.

Pena Murillo, C., Huang, X., Hills, A., McGurk, M., Lyons, A., Jeannon, J.P., Odell, E., Brown, A., Lavery, K., Barrett, W., et al. (2012). The utility of molecular diagnostics to predict recurrence of head and neck carcinoma. Br. J. Cancer *107*, 1138–1143.

Sansregret, L., and Swanton, C. (2017). The role of aneuploidy in cancer evolution. Cold Spring Harb. Perspect. Med. *7*, pii: a028373.

Schindelin, J., Arganda-Carreras, I., Frise, E., Kaynig, V., Longair, M., Pietzsch, T., Preibisch, S., Rueden, C., Saalfeld, S., Schmid, B., et al. (2012). Fiji: an open-source platform for biological-image analysis. Nature Methods *9*, 676–682, 2012.

Schramek, D., Sendoel, A., Segal, J.P., Beronja, S., Heller, E., Oristian, D., Reva, B., and Fuchs, E. (2014). Direct in vivo RNAi screen unveils myosin IIa as a tumor suppressor of squamous cell carcinomas. Science *343*, 309–313.

Talmadge, J.E., and Fidler, I.J. (2010). AACR centennial series: the biology of cancer metastasis: historical perspective. Cancer Res. *70*, 5649–5669.

Thielecke, L., Aranyossy, T., Dahl, A., Tiwari, R., Roeder, I., Geiger, H., Fehse, B., Glauche, I., and Cornils, K. (2017). Limitations and challenges of genetic barcode quantification. Sci. Rep. *7*, 43249.

Turajlic, S., and Swanton, C. (2016). Metastasis as an evolutionary process. Science *352*, 169–175.

Van der Auwera, G.A., Carneiro, M.O., Hartl, C., Poplin, R., Del Angel, G., Levy-Moonshine, A., Jordan, T., Shakir, K., Roazen, D., Thibault, J., et al. (2013). From FastQ data to high confidence variant calls: the Genome Analysis Toolkit best practices pipeline. Curr. Protoc. Bioinformatics *43*, 11.10.11–33.

van Ginkel, J.H., de Leng, W.W., de Bree, R., van Es, R.J., and Willems, S.M. (2016). Targeted sequencing reveals TP53 as a potential diagnostic biomarker in the post-treatment surveillance of head and neck cancer. Oncotarget *7*, 61575–61586.

Weber, K., Bartsch, U., Stocking, C., and Fehse, B. (2008). A multicolor panel of novel lentiviral "gene ontology" (LeGO) vectors for functional gene analysis. Mol. Ther *16*, 698–706.

Weber, K., Thomaschewski, M., Warlich, M., Volz, T., Cornils, K., Niebuhr, B., Täger, M., Lütgehetmann, M., Pollok, J.M., Stocking, C., et al. (2011). RGB marking facilitates multicolor clonal cell tracking. Nat. Med. *17*, 504–509.

Weber, K., Thomaschewski, M., Benten, D., and Fehse, B. (2012). RGB marking with lentiviral vectors for multicolor clonal cell tracking. Nat. Protoc. *7*, 839–849.

Wheeler, S.E., Shi, H., Lin, F., Dasari, S., Bednash, J., Thorne, S., Watkins, S., Joshi, R., and Thomas, S.M. (2014). Enhancement of head and neck squamous cell carcinoma proliferation, invasion, and metastasis by tumor-associated fibroblasts in preclinical models. Head Neck *36*, 385–392.

Wickham, H. (2009). Ggplot2: Elegant Graphics for Data Analysis (Springer).

Wilm, A., Aw, P.P., Bertrand, D., Yeo, G.H., Ong, S.H., Wong, C.H., Khor, C.C., Petric, R., Hibberd, M.L., and Nagarajan, N. (2012). LoFreq: a sequence-quality aware, ultra-sensitive variant caller for uncovering cell-population heterogeneity from high-throughput sequencing datasets. Nucleic Acids Res. *40*, 11189–11201.

Ye, X., and Weinberg, R.A. (2015). Epithelial-mesenchymal plasticity: a central regulator of cancer progression. Trends Cell Biol. *25*, 675–686.

Zhang, Z., Dong, Z., Lauxen, I.S., Filho, M.S., and Nör, J.E. (2014). Endothelial cell-secreted EGF induces epithelial to mesenchymal transition and endows head and neck cancer cells with stem-like phenotype. Cancer Res. *74*, 2869–2881.

Zougman, A., Selby, P.J., and Banks, R.E. (2014). Suspension trapping (STrap) sample preparation method for bottom-up proteomics analysis. Proteomics *14*, 1006.

STAR★METHODS

KEY RESOURCES TABLE

REAGENT or RESOURCE	SOURCE	IDENTIFIER
Antibodies		
Rat anti-mouse Lyve-1 monoclonal antibody	R and D Systems	Cat#MAB2125; RRID:AB_2138528
Goat anti Vimentin (Ab-247)	Home made	Hartig et al., 1997
Rabbit anti E-Cadherin (24E10) monoclonal antibody	Cell Signaling Technology	Cat# 3195; RRID:AB_2291471
Rabbit anti SLUG (C19G7) monoclonal antibody	Cell Signaling Technology	Cat# 9585; RRID:AB_2239535
Rabbit anti ZEB1 (D80D3) monoclonal antibody	Cell Signaling Technology	Cat# 3396; RRID: AB_1904164
Rabbit anti EGFR polyclonal antibody	Cell Signaling Technology	Cat# 2232; RRID: AB_823483
Rabbit anti phospho-EGFR (Tyr1068) polyclonal antibody	Cell Signaling Technology	Cat# 2234; RRID: AB_331701
Mouse anti CD10 (clone A12/G4)	Dr. D. Rimoldi (LICR)	NA
Mouse anti SMAD4 (B-8) monoclonal antibody	Santa Cruz Biotechnology	Cat# sc-7966; RRID: AB_627905
Rabbit anti phospho-SMAD2 (Ser465/467) monoclonal antibody (138D4)	Cell Signaling Technology	Cat# 3108; RRID: AB_490941
Mouse anti GAPDH (clone 6C5)	Millipore	Cat#MAB374; RRID:AB_2107445
Mouse anti CD10 coupled with PE-Cy7	Biolegend	312214, RRID:AB_2146548
Bacterial and Virus Strains		
LeGO-V2 (Venus)	Weber et al., 2008	Addgene Plasmid #27340
LeGO-Cer2 (Cerulean)	Weber et al., 2008	Addgene Plasmid #27338
LeGO-C2 (mCherry)	Weber et al., 2008	Addgene Plasmid #27339
LeGO-eBFP2-2A-Puro-BC32	This paper	Thielecke et al., 2017
pBabe-hTERT	Prof. G.-P. Dotto (UNIL)	N/A
Chemicals, Peptides, and Recombinant Proteins		
PF-02341066(Crizotinib)	Active Biochem	Cat#A-1031
Critical Commercial Assays		
Q5 DNA polymerase	NEB	Cat#M0491S
NEBNext® Multiplex Oligos for Illumina® kits	NEB	Cat#E7335, Cat#E7500, Cat#E6609
Deposited Data		
Fastq sequences from explant cell line exomes	This paper	ENA #PRJEB25375
Data processing scripts	This paper	https://github.com/vroh/BC32_BarSeq
Experimental Models: Cell Lines		
Human: CAL27 (tongue squamous cell carcinoma, male)	ATCC	CRL-2095™
Human: CRGB (derived from CAL27)	This paper	N/A
Human: RGB32 (derived from CRGB)	This paper	N/A
Human: 293R (derived from RGB32)	This paper	N/A
Human: 407R (derived from RGB32)	This paper	N/A
Human: 411R (derived from RGB32)	This paper	N/A
Human: 578R (derived from 293R)	This paper	N/A
Human: 581R-A (derived from 407R)	This paper	N/A
Human: 581R-LNM (derived from 407R)	This paper	N/A
Human: 582R (derived from 407R)	This paper	N/A
Human: 584R (derived from 411R)	This paper	N/A
Human: 585R (derived from 411R)	This paper	N/A
Human: 411R/VeHi (derived from 411R)	This paper	N/A
Human: 411R/VeLo (derived from 411R)	This paper	N/A

(*Continued on next page*)

Continued

REAGENT or RESOURCE	SOURCE	IDENTIFIER
Human: RGB32_CD10^{hi}/PE^{low} (derived from RGB32)	This paper	N/A
Human: RGB32_CD10^{hi}/PE^{hi} (derived from RGB32)	This paper	N/A
Human: RGB32_CD10^{hi} (derived from RGB32_CD10^{hi}/PE^{low} and RGB32_CD10^{hi}/PE^{hi})	This paper	N/A
Human: RGB32_CD10^{low} (derived from RGB32)	This paper	N/A
Human: 673 (derived from RGB32_CD10^{hi})	This paper	N/A
Human: 673R (derived from RGB32_CD10^{hi})	This paper	N/A
Human: 677 (derived from RGB32_CD10^{hi})	This paper	N/A
Human: cancer associated fibroblasts CAFs	This paper	N/A
Human: immortalized cancer associated fibroblasts CAF-T (derived from CAFs)	This paper	N/A
Experimental Models: Organisms/Strains		
Mouse: NMRI/Nude (female)	JANVIER LABS	RjOrl:NMRI-Foxn1nu /Foxn1nu
Oligonucleotides		
MPLX-sPCR1: ACACTCTTTCCCTACACGACGCTC TTCCGATC-s-t	This paper	N/A
MPLX-sPCR2: GTGACTGGAGTTCAGACGTGTGCTC TTCCGATC-s-t	This paper	N/A
ZEB1-Q1F: TTACACCTTTGCATACAGAACCC	This paper	N/A
ZEB1-Q2R: TTTACGATTACACCCAGACTGC	This paper	N/A
SNAI2-Q1: CGAACTGGACACACATACAGTG	This paper	N/A
SNAI2-Q2: CTGAGGATCTCTGGTTGTGGT	This paper	N/A
GAPDH-Q1: ATGGGGAAGGTGAAGGTCG	This paper	N/A
GAPDH-Q2: GGGGTCATTGATGGCAACAATA	This paper	N/A
BarSeq-Sanger1: ACACTCTTTCCCTACACGAC	This paper	N/A
BarSeq-Sanger2: GTGACTGGAGTTCAGACGTG	This paper	N/A
Software and Algorithms		
Fiji	Schindelin et al., 2012	https://fiji.sc/
R	R Foundation for Statistical Computing	https://www.R-project.org
PRISM	GraphPad	https://www.graphpad.com

CONTACT FOR REAGENT AND RESOURCE SHARING

Further information and requests for reagents may be directed to, and will be fulfilled by the Lead Contact, Genrich V. Tolstonog (genrich.tolstonog@chuv.ch).

EXPERIMENTAL MODEL AND SUBJECT DETAILS

Mice

All mouse experiments were approved by the Ethics Committee for Animal Experimentation of Switzerland and performed following institutional guidelines. Eight-week-old female NMRI/Nude mice (JANVIER LABS, Le Genest-Saint-Isle, France) were used to generate HNSCC tumors growing in the submental region as previously described (Behren et al., 2010). Cell implantation, microsurgical tumor resection, treatment with Crizotinib (PF-02341066, Active Biochem) and postsurgical follow-up including tumor sampling for histology, microscopy and barcode analysis are described below.

Cell culture and generation of cell lines

Human CAL27 (ATCC CRL-2095) cell line was purchased from ATCC and authenticated by STR profiling (Microsynth). CRGB cell line was generated using our established protocol for RGB marking (Weber et al., 2011, 2012). RGB32 cell line was derived from CRGB cell line by lentiviral transduction with a library of LeGO-eBFP2-2A-Puro-BC32 high-complexity DNA barcodes. Detailed protocols for generation of CRGB and RGB32 cell lines, explant cell lines from tumor-bearing mice and cell lines sorted by FACS are provided in the Method Details.

METHOD DETAILS

Generation of barcoded cells (see also Figure S6A)

Parental and derivate cell lines were maintained in DMEM + GlutaMAX (GIBCO 31966) supplemented with 10% FBS (GIBCO 10270106) in a humidified atmosphere of 5% CO_2 at 37°C. CRGB were generated from CAL27 using our established protocol for RGB marking (Weber et al., 2011, 2012). In brief, high-titer preparation of LeGO vectors encoding mCherry, Venus, or Cerulean were produced as described (Weber et al., 2008, 2012). CAL27 were plated at 0.5 × 10^6 cells/well in 6-well plates, and a total of 18 × 10^6 cells were subjected to RGB marking (day 1). At day 4, cells were pooled and analyzed for fluorescent protein expression by flow cytometry. Frequencies were: 56.3% mCherry$^+$, 51.2% Venus$^+$ and 48.1% Cerulean$^+$, indicating optimal RGB labeling. Pooled cells were expanded in T75 cell culture flasks. At day 12, RGB-marked CAL27 were again pooled and fluorescence-positive (red *or* green *or* blue) cells were sorted by FACS (> 99% purity). On day 19, 12 × 10^6 CRGB cells were transduced with a library of LeGO-eBFP2-2A-Puro-BC32 high-complexity DNA barcodes. The vector library was generated as described (Thielecke et al., 2017). To facilitate detection and selection of successfully transduced cells, this new barcoding vector encodes a blue fluorescent protein (eBFP) coupled to a puromycin resistance gene via a 2A sequence. At day 22, a transduction efficiency of 4% was determined based on eBFP expression indicating single vector integrations (Kustikova et al., 2003), i.e., unique barcodes in each cell. Resulting barcoded RGB-labeled CAL27 (designated as RGB32) were selected with puromycin.

Based on the data from the previous RGB marking and titration experiments (not shown), it has been clear that CAL27 cells are easy-to-transduce. In fact, transduction was readily titratable over a wide linear range. As previously shown, based thereon it can be concluded that vector-copy-numbers follow a Poisson distribution (Fehse et al., 2004). Thus, at the low transduction rate of 4% used, there is a very little likelihood that any transduced cell contains more than one vector copy (Kustikova et al., 2003). To obtain a pure population of barcoded cells, transduced cells were selected by puromycin treatment, which, however, could not impact the vector copy number per cell. Moreover, we propose that double-barcoding would be evident by an equal, closed to 50:50, ratio of two barcodes, but we don't have indications for either bi- or poly-barcoding events. Barcode monoclonality in the 2nd-generation explant cell lines is in favor of a single integration. To assess barcodes numbers empirically, we performed digital droplet PCR (ddPCR) for copy number analysis of integrated barcodes in RGB32 cell line. A duplex assay against Illumina (i.e., BC32) sequences and the human *EpoR* gene (chromosome 19) as a reference was performed. The ddPCR data clearly showed that on average there was one (1.04) barcode present per two *EpoR* copies. Allowing a 10% error for ddPCR, the copy number would be between 0.94 and 1.14 per two *EpoR* genes. The data clearly demonstrated that RGB32 cells (or at least the vast majority of cells in the barcoded population) contained 1 barcode, as expected.

Generation of explant cell lines (see also Figure S6A)

To establish explant cell lines from tumor-bearing mice, tumors (or lymph nodes) collected in saline were immediately incubated twice 5 minutes in Betadine (Mundipharma), washed twice in PBS, minced and maintained in DMEM + GlutaMAX and 10% FBS supplemented with Penicillin (100 IU/ml), Streptomycin (100 μg/ml) (BioConcept 4-01F00-H) and Amphotericin B (2.5 μg/ml) (GIBCO 15290026). Explant cell lines 293R, 407R and 411R were isolated from a series of recurrent tumors developing after surgical resection of primary tumors generated by implantation of RGB32 cells in mice. Explant cell lines 578R, 581R-A, 582R, 584R and 585R were isolated from recurrent tumors developing after surgical resection of tumors resulting from re-implantation of 293R, 407R or 411R explants. Explant 581R-LNM was isolated from a lymph node metastasis following re-implantation of explant 407R.

Generation of cell lines by cell sorting

RGB32 cells were sorted in 3 separate fractions on a BD FACSAria III cell sorter at the Ludwig's Flow Cytometry Facility using an anti-CD10 antibody coupled to PE-Cy7 (Biolegend #312214) and the PE filter to measure mCherry positivity. This resulted in the generation of CD10^{high}/PE^{low}, CD10^{high}/PE^{high} and CD10^{low} cells. CD10^{high}/PE^{low} and CD10^{high}/PE^{high} cells were mixed in accordance to their original sorting ratio in order to reconstitute CD10^{high} cells.

Cell culture of CAFs

Human cancer associated fibroblasts were established from a tumor biopsy from a patient undergoing surgery at the CHUV. The procedure was approved by the Cantonal Department of the Swiss Ethics Committees and the relevant informed consent form was signed by the patient. CAFs were cultured in DMEM/F-12 + GlutaMAX (GIBCO 31331028) supplemented with 10% FBS. Established CAFs were transduced with pBabe-hTERT vector (kindly provided by Prof. G.-P. Dotto, UNIL) to generate immortalized CAF-T cells.

Organotypic cell culture

Collagen plugs were prepared by mixing DMEM + GlutaMAX and 10% FBS with Collagen I (Ibidi # 50205) to a final concentration of 2.8 mg/ml. Collagen was neutralized with NaOH (10 mM final) and 1 mL of collagen solution was transferred into a well from a 24-well plate (TPP # 92424) and incubated at 37°C for 30 minutes to allow the gel to set. 2x10^5 CAF-T cells were mixed with 1.6x10^5 CAL27 and either 4x10^4 RGB32 or 407R cells. The cell solution was then seeded on top of the collagen plug and incubated overnight. The plugs were transferred on collagen-coated nylon discs placed on top of a metal grid inside a poly-HEMA (Sigma-Aldrich) coated 6 cm

dish (TPP # 93060) filled with culture medium. The organotypes were allowed to develop for 13 days in culture before collection in 4% PFA/PBS and processing as described below for tumor samples.

Surgical mouse model of HNSCC tumors

Human HNSCC cells (CAL27, RGB32, 293R, 407R, 411R, $CD10^{high}$ or $CD10^{low}$) were resuspended in 30 μL HBSS (GIBCO 14175053) with or without addition of CAFs (see details in Figure S6B). The cell solution was mixed on ice with 20 μL BD Matrigel (Becton Dickinson 356234) and subcutaneously injected along the submental midline of 8-week-old female NMRI/Nude mice (JANVIER LABS, Le Genest-Saint-Isle, France) to generate HNSCC tumors. Tumor volume was monitored using a Vernier caliper and calculated using the modified ellipsoid formula: Volume = 1/2 * (Length * $(Width)^2$). When primary tumors reached about 200-250 mm^3, mice underwent microsurgical tumor resection under general anesthesia. One day before surgery, paracetamol (Dafalgan; 2 mg/ml) was provided in drinking water. Right before surgery, mice were anesthetized by intraperitoneal injection of a mixture of ketamine (50 mg/kg) and medetomidine (Dorbene; 1 mg/kg). Resection of tumors was performed using iris scissors and microsurgical bipolar forceps (Erbotom; ERBE SWISS AG). This surgical operation included a precise control of the surgical tumor bed by fluorescence imaging of tumor cells using a Nikon SMZ1270i stereomicroscope. Tumors were dissected in pieces that were either collected by snap freezing in liquid nitrogen for downstream DNA extraction and barcode analysis (Bar-Seq; see below) or further processed for histological evaluation, fluorescence imaging (spectral analysis of RGB colors) and immunostainings. For experiments exploring the dissemination of cancer cells beyond the border of the tumor, the adjacent muscles were dissected and collected in liquid nitrogen. The enrichment score reported in Figure 3F was calculated by the log ratio of barcode counts (incremented by 0.01 pseudo-count) in the muscle compared to the counts in the matching tumor. Wounds were closed with multifilament, 6.0 polyglycolic acid sutures (B. Braun Medical SA, C0049607). Thereafter, 0.5 mL warm 0.9% NaCl was injected intraperitoneally and atipamezole (Alzane; 2.5 mg/kg) was injected subcutaneously to antagonize medetomidine. Afterward, buprenorphine (0.05 mg/kg) was administrated subcutaneously, and the mouse was placed on a heating pad until full recovery. During 7 days post-surgery, mice were treated with enrofloxacin (600 mg/L) and paracetamol (Dafalgan; 2 mg/ml) in drinking water. Wounded skin was treated with Bepanthen cream until completion of healing. Eight pairs were available for the analysis of matched primary and recurrent tumors (see details provided in Figure S6C).

Crizotinib treatment of tumor-bearing animals

From 14 days post-implantation up to the day of surgery (e.g., neo-adjuvant treatment), CAL27 tumor-bearing mice were treated daily by gavage with 12.5 mg/kg Crizotinib (PF-02341066, Active Biochem) diluted in drinking water (containing DMSO at a final concentration of 1%). Mice additionally received a second treatment by gavage with 12.5 mg/kg Crizotinib diluted in drinking water from day 10 to 20 post surgery. Control mice only received the vehicle (1% DMSO, Sigma #41639). For this experiment (Figure S4I) a Log-rank (Mantel-Cox) test was computed in GraphPad PRISM to determine the statistical significance level of the observed recurrence-free survival benefit.

Histology and Immunofluorescence

For hematoxylin and eosin staining, tumors were fixed in formalin 10% (Sigma-Aldrich, HT501128) before embedding into paraffin. For (immuno)fluorescence microscopy evaluation, tumors were fixed overnight in 4% paraformaldehyde (PFA) in PBS and transferred into 30% sucrose for a minimum of 4 hours before embedding into O.C.T. Compound Tissue-Tek (Sakura Finetek). For Lyve-1 (RnD # mab-2125) and vimentin (Ab-247 (home-made) [Hartig et al., 1997]) immunostaining, PFA-fixed sections were permeabilized 10 minutes at RT with 0.1% Triton X-100 then blocked 30 minutes in PBS 0.5% BSA containing either 1% goat serum (for Lyve-1) or 1% donkey serum (for vimentin) before incubation for 1 h at RT with primary antibodies diluted (1/200 respectively 1/1000) in Dako background-reducing agent (#S302283). After incubating 1 h at RT with secondary antibodies (goat anti-rat-A647 (Life technologies A-21247) or donkey anti-goat-A647 (Life technologies A-21447)) diluted 1/500 in Dako background-reducing agent, sections were mounted in ProLong Gold antifade reagent with DAPI (Life technologies P-36931) and evaluated by fluorescence microscopy. Immunofluorescence on cell lines was performed with antibodies raised against SLUG (Cell signaling, C19G7 Rabbit mAb #9585) and ZEB1 (Cell signaling, D80D3 Rabbit mAb #3396).

DNA extraction and BC32 barcode retrieval

Genomic DNA (gDNA) was extracted from tumor tissue or cell pellets using QIAamp DNA mini kit (QIAGEN # 51304) following manufacturer instructions and including a digestion step with proteinase K (Applichem # A4392). DNA was eluted in 10 mM Tris-HCl (pH 8.0). Extraction of DNA from muscle was performed with QiaAmp Fast DNA tissue kit (QIAGEN # 51404), and DNA was eluted in manufacturer's buffer ATE.

Starting with 200 ng (tumor or cell gDNA) or 1 μg (muscle gDNA) of template, barcodes from tumor or cell lines were retrieved by 30 PCR cycles (5min 95°C, 30x [30 s 95°C, 30 s 57°C, 30 s 72°C], 10min 68°C) using high-fidelity Q5 DNA polymerase (NEB M0491S) and index primers from the NEBNext Multiplex Oligos for Illumina kits (NEB E7335, E7500 and E6609) to allow multiplexing of samples. Barcode products were then purified with Agencourt AMPure XP beads (#A63880) using a one-step protocol with a beads ratio of 1.8x. For muscle DNA samples, barcodes were first pre-amplified by 15-30 PCR cycles using custom primers with phosphorothioate bonds (MPLX-sPCR1: ACACTCTTTCCCTACACGACGCTCTTCCGATC-s-t, MPLX-sPCR2: GTGACTGGAGTTCAGACGTGTGCTCTTCCGATC-s-t). Pre-amplified barcodes were purified with AMPure XP beads using a two-step protocol with beads ratios of 0.9x and

1.8x successively. Muscle gDNA derived barcodes were then indexed with 25 additional PCR cycles using NEBNext Multiplex Oligos for Illumina and purified with AMPure XP beads (one-step protocol at 1.8x ratio). Library quality and fragment sizes were assessed on a Fragment Analyzer (Advanced Analytical) before high-throughput sequencing on a MiSeq platform (Illumina) at the Genomic Technologies Facility (GTF) of the University of Lausanne or on a MiniSeq platform (Illumina) at the Ludwig Institute for Cancer Research in Lausanne. When a sample was expected to be monoclonal, purified barcodes were eventually sequenced by the conventional Sanger method (Eurofins Genomics) to manage costs.

To ensure that the proof-reading activity of the Q5 DNA polymerase prevents barcode bias during PCR, amplification of an artificial barcode-like template was controlled by NGS and showed a nearly constant low-rate of PCR errors even after 60 cycles (Figure S1D).

Laser microdissection

PFA-sucrose-OCT cryosections from five primary tumors where processed using Arcturus^{XT} laser capture microdissection system (Applied Biosystem). Each specimen was cut in two successive radial areas from the center of the tumor to the periphery of the tumor, and for each of the regions three serial sections were manually collected and pooled together after dissection by UV laser. Microdissected sections were reverse-crosslinked by overnight incubation at 65°C in 200 μL ChIP elution buffer (50 mM Tris-HCl pH 8.0, 1% SDS, 10 mM EDTA). The next day, 3.5 μL of 300 mM $CaCl_2$ in 10 mM Tris pH 8.0 and 2 μL of 20 mg/ml Proteinase K were added to the solution and further incubated for 2 hours at 50°C before DNA extraction using NucleoSpin Gel and PCR Clean-up kit (Macherey-Nagel AG, #740609.5). 1 μg of carrier mouse DNA was added to enhance purification. DNA samples were then normally processed for barcode retrieval and NGS library preparation.

RNA isolation and RT-qPCR

Total RNA from cell cultures was extracted with TRI Reagent (Sigma T-9424) and purified using Direct-zol RNA MiniPrep (Zymo Research R2052) including a digestion step with DNase I (Roche 04 536 282 001). RNA (1 μg) was converted into cDNA using the High Capacity RNA-to-cDNA Kit (Applied Biosystems, 4368814). Expression of *ZEB1* or *SNAI2* genes was quantified on an ABI 7500 Fast Real-Time PCR machine using Fast SYBR Green Master Mix (Applied Biosystems #4385618), 10 ng of template cDNA and the following primer pairs at 0.2 μM: ZEB1-Q1F (5′-TTACACCTTTGCATACAGAACCC-3′) and ZEB1-Q2R (5′-TTTACGATTAC ACCCAGACTGC-3′), or SNAI2-Q1 (5′-CGAACTGGACACACATACAGTG-3′) and SNAI2-Q2 (5′-CTGAGGATCTCTGGTTGTGGT-3′). To calculate relative expression (RE) in each sample (compared to CAL27 expression), we used the formula $RE = 2^{-(\Delta\Delta Ct)}$ were ΔΔCt corresponds to ($\Delta Ct^{sample} - \Delta Ct^{CAL27}$) with ΔCt being the Ct value of the target gene after normalization to *GAPDH* Ct value (Ct_{gene} - Ct_{GAPDH}). *GAPDH* was detected using the primers GAPDH-Q1 (5′-ATGGGGAAGGTGAAGGTCG-3′) and GAPDH-Q2 (5′-GGGGTCATTGATGGCAACAATA-3′).

Immunoblotting

Protein lysates were prepared in KLB lysis buffer supplemented with protease and phosphatase inhibitors (25 mM Tris-HCl (pH 7.4), 150 mM NaCl, 5 mM EDTA, 10% glycerol, 1% Triton X-100, 10 mM sodium pyrophosphate, 10 mM β-glycerophosphate, 1 mM Pefabloc SC (Roche 11 429 868 001), 0.02 mg/ml aprotinin, 10 mM sodium fluoride, 1 mM sodium orthovanadate) and were separated by SDS-PAGE before transfer onto nitrocellulose Hybond membranes (GE / Amersham 10600003). After a blocking step with 5% nonfat dry milk in PBS + 0.1% Tween 20 (PBS-T), membranes were incubated overnight with any of the following primary antibodies diluted in PBS-T + 2.5% milk: E-Cadherin (Cell Signaling 3195), EGFR (Cell Signaling 2232), phospho-EGFR (Tyr1068) (Cell Signaling 2234), SMAD4 (Santa Cruz 7966) and phospho-SMAD2 (Ser465/467) (Cell Signaling 3108) all at 1/1'000, GAPDH at 1/40'000 (Merck Millipore MAB374) and CD10 at 1/10 (hybridoma supernatant A12/G4, gift from Dr. Donata Rimoldi). HRP-conjugated secondary antibodies (anti-mouse: DAKO P026002-2, anti-rabbit: DAKO P044801) were diluted at 1/5′000 in PBS-T + 2.5% milk and the signal was detected on a Vilber Fusion FX imager after incubation with Radiance Plus femtogram HRP Substrate (azure biosystems AC2103) or SuperSignal West Pico Chemiluminescent Substrate (Thermo Scientific 34087). Quantification of bands was performed using Image Studio Lite Ver 5.2 (LI-COR Biosciences) and Fiji (https://fiji.sc/).

Sanger sequencing

Sanger sequencing of PCR products was performed by Eurofins Genomics (Ebersberg, Germany). Chromatogram profiles were inspected using sangerseqR package (v. 1.6.0) (Hill et al., 2014).

Analysis of BC32 barcode sequences (Bar-Seq)

BC32 barcodes consist of a repetitive motif of 3 fixed nucleotides followed by 2 random nucleotides producing the subsequent backbone sequence: 5′-CTA NN CAG NN CTT NN CGA NN CTA NN CTT NN GGA NN CTA NN CAG NN CTT NN CGA NN CTA NN CTT NN GGA NN CTA NN CAG NN-3′. The BC32 barcode construct is based on mCherry-BC16 (Cornils et al., 2014) and follows the optimization previously described (Thielecke et al., 2017). The structure of the LeGO-eBFP2-2A-Puro-BC32 vector used in this study is identical to the one shown in Thielecke et al. (2017), but the marker gene was replaced by a eBFP-2a-Puro cassette. The complete vector sequence is available upon request to Kerstin Cornils and Boris Fehse.

Sequence processing and analysis were performed in R (https://www.R-project.org). All functions required for our Bar-Seq analysis pipeline are provided in the BC32BarSeq package readily accessible on GitHub (see availability below). For the processing,

reads that did not strictly match their expected multiplex index sequence (including 5 additional upstream and downstream constant bases) were filtered out to avoid cross-sample contamination resulting from potential de-multiplexing errors. Next, reads matching the BC32 backbone sequence (allowing for one substitution and/or one indel) were selected for downstream analysis. After careful review of the sequences failing at the index or barcode matching step, some important additional barcode sequences were manually authorized for downstream analysis when deemed necessary (e.g., for major clones differing from the barcode pattern by more than one substitution).

These initial filtering steps were performed with ShortRead (v. 1.34.1) (Morgan et al., 2009) and BioString (v. 2.44.2). For each sample, the total number of read counts for each distinct BC32 sequence identified was then calculated. For clarity, we have arbitrarily attributed a unique short name to each barcode (R1, ..., Rn) mainly based on their rank after sorting by decreasing frequency in the parental cell line. The PCR error rate inherent to our system was evaluated in a cell-free environment limiting the rate of natural mutations. To do so, a "barcode-like" synthetic oligonucleotide was designed by selecting a low occurrence BC32 real barcode and shuffling its fixed-nucleotides triplets. The resulting oligonucleotide 5′-CTA AAC AGA GCT ATG CTT GGC AGT TCT TCC CTA ATC TTA CGG AGG CAG GTC GAG GGG ACT CTA CAC GAA GCT AAG CTT CT-3′ was amplified by 30, 45 or 60 PCR cycles using 1 ng of template and multiplexing primers. The resulting PCR products were purified and sequenced on a MiSeq machine. The percentage of sequencing reads deviating from the oligonucleotide reference remained nearly constant despite the increasing number of PCR cycles. For each sequenced sample, we used stringdist (v. 0.9.4.6) to calculate the restricted Damerau-Levenshtein distance matrix between sequences and pooled any group of sequences differing by 12 or less mismatches under one individual barcode ID. To optimize computation time, these initial processing steps were parallelized on Vital-IT (https://www.vital-it.ch/) cluster computers (Vital-IT Center for high-performance computing of the Swiss Institute of Bioinformatics). For a global data analysis, barcode counts for each sample were merged in one summary table (Table S1). To reduce noise, any read count below 10 was substituted by 0. Finally, sample-wise frequencies and counts per million (CPMs) have been calculated for each barcode. Most plots were generated using ggplot2 (v. 2.2.1) (Wickham, 2009), except Venn diagrams using VennDiagram (v. 1.6.17) and heatmaps using gplots (v. 3.0.1). Dplyr (v. 0.7.2) and reshape2 (v. 1.4.2) were commonly used for data tidying purposes. Additional details on the Bar-Seq processing can be found in the BC32BarSeq vignette.

Fluorescence imaging and spectral analysis

Eight-μm sections were cut from PFA/Sucrose/OCT embedded tumors (Mouse Pathology Facility, Lausanne) and mounted with a coverslip using ProLong Diamond Antifade mounting media (Molecular Probes P36965). Sections were imaged with a Zeiss Axio Imager Z1 microscope using fluorescence filters (Cellular Imaging Facility, Lausanne). Color spectrum graphs for each tumor image were obtained with the color inspector 3D plugin (http://home.htw-berlin.de/~barthel/ImageJ/ImageJ.htm) from Fiji using a top view of the Hue Saturation Brightness (HSB) display with frequency weight set at maximum and perspective set at zero. This results in a deconvoluted spectrum plot where each pixel from the original picture is plotted according to its hue value on the azimuthal coordinate and its color saturation value on the radial coordinate. Black and white masks of the color spectra from matching primary and recurrent tumors were further colored and merged using "mix RGB" nodes from Blender compositor (https://www.blender.org) with blend types set as screen or multiply respectively. A mask for the overlap between primary and recurrent tumors was generated using a "mix RGB" node with blend type set as subtract on the previously merged images. Finally, quantification of the primary, recurrent and overlapping binary masks was performed in R with a custom script computing the sum of all black pixels in each mask.

Exome sequencing, variants and copy number variation analysis

Exome sequencing was performed on 3 control cell lines (CAL27, RGB, BC32), 11 recurrence-derived explant cell lines (293R, 407R, 411R, 411R/VeHi, 411R/VeLo, 578R, 581R-A, 581R-LNM, 584R, 585R and 673R) and one primary tumor derived explant cell line (673). Variant calling has been performed using the standard BWA-Picard-GATK pipeline. Briefly, exomes were captured using Agilent SureSelect Human All Exon v5 enrichment kits and sequenced on Illumina HiSeq 2500 platform (for control cell lines and 293R, 407R, 411R explant cell lines) or HiSeq 4000 platform (for all other explant cell lines). Purity-filtered reads were trimmed for adapters and quality with FastqM*cf.* (v. 1.1.2, https://github.com/ExpressionAnalysis/ea-utils), and aligned to the human genome (hg19) using BWA-MEM (v. 0.7.12) (Li and Durbin, 2009). BAM files were further processed with GATK (v. 3.7) and LoFreq (v. 2.1.2) (Wilm et al., 2012) for realignment around indels and base quality score recalibration (Van der Auwera et al., 2013). Recalibrated BAM files were then used to detect explant-specific variants with LoFreq. Variants in mitochondrial DNA were called using MuTect2 from the GATK package by explicitly providing "chrM" as the targets interval parameter. *De novo* mutations were called using the reference RGB32 BAM file as normal input (normal run) whereas "wild-typing" genotypes were detected by inverting the inputs hence using RGB32 BAM file as tumor input (reverse run). Reads coverage for each variant position were calculated from recalibrated BAM files using GATK's HaplotypeCaller and custom BED files. Downstream analysis was performed in R. Exome reference BED files (SureSelect V5) were downloaded from Agilent SureDesign website (https://earray.chem.agilent.com/suredesign) and loaded in a GRanges object using GenomicRanges (v. 1.28.4) (Lawrence et al., 2013). The overlap between explant variants and exons referenced in SureSelect V5 BED file was then detected with findOverlap function. Variants were annotated with predictCoding function from the VariantAnnotation package (v. 1.22.3) (Obenchain et al., 2014) using BSgenome.Hsapiens.UCSC.hg19 (v. 1.4.0). Mitochondrial variants were manually annotated. The resulting list of explant-specific variants is available in Table S2.

Copy number analysis was performed on recalibrated BAM files with CODEX (v. 1.8.0) (Jiang et al., 2015) following the default pipeline and settings described in the vignette. Iterating through all chromosomes, normalization of read depth was performed by the normalize2 function with normal_index parameter pointing at CAL27, CRGB and RGB32 samples in order to detect copy number variation under the case-control setting. Segmentation was performed with DNAcopy (v. 1.50.0) with the default settings and using as input the binary log ratios of raw read depth compared to normalized read depth calculated by CODEX (log2(Y/λhat)) after smoothing the data using ksmooth algorithm (R stats package) with a bandwidth parameter $k = 10$. Each segment with a mean variation above 0.2 or below −0.2 was annotated with the names of genes integrated in the segment using GenomicRanges' findOverlap and BSgenome.Hsapiens.UCSC.hg19. Dplyr (v. 0.7.2) and reshape2 (v. 1.4.2) were commonly used for data tidying purposes. The resulting list of explant-specific CNVs is available in Table S3.

Membrane proteomics

Membrane proteomics was performed on three control cell lines (CAL27, CRGB, RGB32) and three recurrent explant cell lines (293R, 407R, 411R) by mass spectrometry at the Clinical and Biomedical Proteomics Group of the University of Leeds. The modified procedure of Bordier for preparation of the enriched membrane protein fractions, the STrap-based tryptic digestion with the following mass spectrometric processing were performed as previously described (Zougman et al., 2014).

QUANTIFICATION AND STATISTICAL ANALYSIS

Mathematical methods

Statistical simulations were done using the statistic software R (Version – 3.4.1) and the binomial functions from the *stats* package. Posterior probabilities were calculated according to a binomial distribution function in which *n* equals the number of remaining tumor cells and p resembling the initial frequency of RTICs within the primary tumor. The simulations were done for an initial RTIC concentration of p = 25% and a surgical tumor removal of 99.9996% of initially 250'000'000 cells (n = 1000). Figure 3D was generated using the statistic software R (Version 3.4.2) and the *stats* package (Version 3.4.2). The two different scenarios were initialized with 400 clones where individual clone sizes were sampled from a Weibull distribution (rweibull). Furthermore, the position of each single cell within the spatially uniform scenario was sampled from a uniform distribution (runif) as well as the seed of each clonal patch within the spatially confined scenario. The individual cells of each clone, making up the patches within the 2nd scenario, were normally distributed around the respective seed (rnorm). We selected a convex hull based on the patchy setting in order to guarantee a compact point cloud (tumor). This boundary was then identically applied to the homogeneous setting. Finally, the convex hull was shrunk so that the "inner mass" of the simulated tumor can be extracted.

Statistics

Statistical parameters including the definitions and exact values of n (e.g., number of samples, number of fields quantified, etc.), distributions and deviations are reported in the figures and corresponding figure legends. Wherever possible, individual data points were overlaid on boxplots to obtain a full representation of the data distribution. Unless otherwise stated, two-sample t tests were used to compute the statistical difference between two groups (in R). Data was judged to be statistically significant when $p < 0.05$.

DATA AND SOFTWARE AVAILABILITY

The R package used to generate a table of counts/frequencies from raw sequence data can be obtained at the following address: https://github.com/vroh/BC32_BarSeq. The accession number for the Fastq files resulting from exome sequencing reported in this paper is European Nucleotide Archive (ENA): PRJEB25375.